




The UV Luminosity Function of Protocluster Galaxies at $z \sim 4$: the Bright-end Excess and the Enhanced Star Formation Rate Density

KEI ITO ^{1,2,3} NOBUNARI KASHIKAWA,³ JUN TOSHIKAWA,^{4,5} RODERIK OVERZIER,^{6,7} MARIKO KUBO,² HISAKAZU UCHIYAMA,² YONGMING LIANG ^{1,2} MASAFUSA ONOUE ⁸ MASAYUKI TANAKA,^{2,1} YUTAKA KOMIYAMA,^{2,1} CHIEN-HSIU LEE,⁹ YEN-TING LIN,¹⁰ MURILO MARINELLO,¹¹ CRYSTAL L. MARTIN,¹² AND TAKATOSHI SHIBUYA¹³

¹*Department of Astronomical Science, The Graduate University for Advanced Studies, SOKENDAI, Mitaka, Tokyo, 181-8588, Japan*

²*National Astronomical Observatory of Japan, Mitaka, Tokyo, 181-8588, Japan*

³*Department of Astronomy, School of Science, The University of Tokyo, 7-3-1 Hongo, Bunkyo-ku, Tokyo, 113-0033, Japan*

⁴*Institute for Cosmic Ray Research, The University of Tokyo, 5-1-5 Kashiwa-no-Ha, Kashiwa, Chiba, 277-8582, Japan*

⁵*Department of Physics, University of Bath, Claverton Down, Bath, BA2 7AY, UK*

⁶*Observatório Nacional, Rua José Cristino, 77. CEP 20921-400, São Cristóvão, Rio de Janeiro-RJ, Brazil*

⁷*Institute of Astronomy, Geophysics and Atmospheric Sciences, Department of Astronomy, University of São Paulo, São Paulo, SP 05508-090, Brazil*

⁸*Max-Planck-Institut für Astronomie, Königstuhl 17, D-69117 Heidelberg, Germany*

⁹*National Optical Astronomy Observatory 950 N Cherry Avenue, Tucson, AZ 85719, USA*

¹⁰*Institute of Astronomy and Astrophysics, Academia Sinica, Taipei 10617, Taiwan*

¹¹*Laboratório Nacional de Astrofísica - Rua dos Estados Unidos 154, Bairro das Nações, CEP 37504-364, Itajubá, MG, Brazil*

¹²*Department of Physics, University of California, Santa Barbara, CA 93106, USA*

¹³*Kitami Institute of Technology, 165 Koen-cho, Kitami, Hokkaido 090-8507, Japan*

(Accepted July 1, 2020)

Submitted to ApJ

ABSTRACT

We report the rest-frame ultraviolet luminosity function of g -dropout galaxies in 177 protocluster candidates (PC UVLF) at $z \sim 4$ selected in the Hyper Suprime-Cam Subaru Strategic Program. Comparing with the UVLF of field galaxies at the same redshift, we find that the PC UVLF shows a significant excess towards the bright-end. This excess can not be explained by the contribution of only active galactic nuclei, and we also find that this is more significant in higher dense regions. Assuming that all protocluster members are located on the star formation main sequence, the PC UVLF can be converted into a stellar mass function. Consequently, our protocluster members are inferred to have a 2.8 times more massive characteristic stellar mass than that of the field Lyman break galaxies at the same redshift. This study, for the first time, clearly shows that the enhancement in star formation or stellar mass in overdense regions can generally be seen as early as at $z \sim 4$. We also estimate the star formation rate density (SFRD) in protocluster regions as $\simeq 6 - 20\%$ of the cosmic SFRD, based on the measured PC UVLF after correcting for the selection incompleteness in our protocluster sample. This high value suggests that protoclusters make a non-negligible contribution to the cosmic SFRD at $z \sim 4$, as previously suggested by simulations. Our results suggest that protoclusters are essential components for the galaxy evolution at $z \sim 4$.

1. INTRODUCTION

Properties of galaxies are known to be correlated to their environments. Galaxies in local clusters tend to be early-type (e.g. Dressler 1980), older (e.g. Thomas et al. 2005), and redder (e.g. Bamford et al. 2008) than galaxies in blank field. However, it is still unclear when and how such environmental trends are shaped. Exploring environmental trends in the early universe, when such

Corresponding author: Kei Ito

kei.ito@grad.nao.ac.jp

onoue@mpia-hd.mpg.de

difference can emerge for the first time, is thus important for solving this long-standing question.

At higher redshifts ($z \geq 2$), we have some overdense regions called protoclusters, which are defined as structures that will collapse into virialized objects with $M_{\text{halo}} \geq 10^{14} M_{\odot}$ at $z \geq 0$ (see Overzier 2016, for a comprehensive review). These structures are not yet virialized, unlike clusters, and most of them consist of star-forming galaxies instead of quiescent ones. Protoclusters have been found through a large variety of selection techniques. In terms of galaxies as tracers of the overdensity, some studies have used line-emitting galaxies such as H α emitters (HAEs) (e.g., Hayashi et al. 2012; Hatch et al. 2011) and Ly α emitters (e.g., Higuchi et al. 2019; Jiang et al. 2018; Toshikawa et al. 2012; Ouchi et al. 2005; Venemans et al. 2002), while others have focused on sub-millimeter galaxies (SMGs) (e.g., Miller et al. 2018), or continuum detected ones such as photo- z selected galaxies (e.g., Chiang et al. 2014) and Lyman break galaxies (LBGs, e.g., Toshikawa et al. 2016; Overzier et al. 2008; Steidel et al. 1998). Also, several studies have used intergalactic medium (IGM) as tracers, such as by Ly α tomography (e.g., Lee et al. 2016; Stark et al. 2015; Lee et al. 2014) or strong coherent Ly α absorption along the line of sight, so-called ‘‘CoSLAs’’ (e.g., Cai et al. 2016).

Protocluster galaxies at $z \sim 2$ have been shown to differ their properties compared to field galaxies at the same epoch. They tend to have enhancements of star formation rates (SFRs) (e.g., Shimakawa et al. 2018; Koyama et al. 2013), with larger stellar mass (above references and Cooke et al. 2014; Hatch et al. 2011; Steidel et al. 2005). This suggests that the galaxy formation is earlier in protoclusters, as supported by several theoretical studies (Chiang et al. 2017; Lovell et al. 2018; Muldrew et al. 2015). Moreover, these theoretical studies suggest that these differences are already in place at even higher redshift. The examination of the galaxy population in protoclusters at higher redshifts is thus crucial for understanding effects of environment.

However, the SFR and the stellar mass of galaxies in overdense regions at $z \geq 3$ have not yet been comprehensively assessed. There are several reasons for this. First, only ~ 20 protoclusters have been found to date at $z \geq 3$ due to their extremely low number density (Overzier 2016), which is insufficient for a systematic study. Second, the target selection is highly heterogeneous: in addition to the variety of tracers of galaxies mentioned above, some studies focus on regions around quasars or radio galaxies (e.g., Hayashi et al. 2012; Venemans et al. 2007), while others focus on blank fields (e.g., Toshikawa et al. 2016; Chiang et al. 2014). Third, the

precise estimation of the stellar mass and SFR through spectral energy distribution (SED) fitting requires the rest-frame optical data. At $z \geq 4$, the rest-frame optical is shifted to the (near) infrared ($\lambda \geq 2.0 \mu\text{m}$) in the observed frame, so observations become much more challenging.

The rest-frame ultraviolet (rest-UV) luminosity function (UVLF) is an effective and practical tool for unraveling the properties of high redshift galaxies. The rest-UV light is generally emitted from short-lived massive stars and thus a good tracer of SFR (Kennicutt 1998). UVLFs of field galaxies as a function of the cosmic time are the dominant diagnostic for understanding the history of cosmic star formation (e.g., Bouwens et al. 2015; Cucciati et al. 2012; van der Burg et al. 2010, and see Madau & Dickinson 2014 for a comprehensive review). In addition, if we apply a relation between the stellar mass and SFR, so-called ‘‘main sequence’’ (e.g., Song et al. 2016; Speagle et al. 2014, and references therein.), UVLFs provide shapes of galaxy stellar mass functions (SMFs). Therefore, estimating a UVLF of protocluster galaxies at $z \geq 3$ will provide us with an opportunity of revealing the general properties of galaxies in high-density regions. On the other hand, an accurate measurement of UVLFs of protoclusters requires a large number of protocluster samples, which has been the biggest obstacle.

Recently, we have conducted a new protocluster survey (Toshikawa et al. 2018, hereafter called T18) from the photometric data of the Hyper Suprime-Cam (HSC) Subaru Strategic Program (HSC-SSP) (Aihara et al. 2018a). Starting with a map of the overdensity of LBGs at $z \sim 4$ (so-called g -dropout galaxies), defined as the difference in the local surface number density of galaxies from its average, we have found 179 protocluster candidates over an area of 121 deg^2 . Based on this sample, we have conducted several follow-up studies, investigating the relation between overdensity and bright QSOs (Uchiyama et al. 2018), and quasar pairs (Onoue et al. 2018), considering the brightest UV-selected galaxies in protoclusters as candidates of proto-brightest cluster galaxies (Ito et al. 2019), and using the stacked infrared (IR) properties of protoclusters to probe obscured star formation and active galactic nuclei (AGNs) (Kubo et al. 2019). The systematic and homogeneous selection combined with the large size of our protocluster sample should also enable us to estimate the general UVLF of protocluster galaxies at $z \sim 4$ for the first time.

In this paper, we present the first measurement of the UVLF of galaxies in protoclusters at $z \sim 4$. The remainder of this paper is organized as follows. We introduce our protocluster sample and their member galaxies in

Section 2 and describe the procedure and results of the measurement of the UVLF in Section 3. The SMF, the variety of UVLF, and the SFR density (SFRD) of their member galaxies inferred from the UVLF are estimated in Section 4. Section 5 examines the validity of this result and discusses the implications for the galaxy formation in overdense regions. We summarize the paper in Section 6. In this paper, we assume that cosmological parameters are $H_0 = 70 \text{ km s}^{-1} \text{ Mpc}^{-1}$, $\Omega_m = 0.3$, and $\Omega_\Lambda = 0.7$. We use the AB magnitude system.

2. DATA SUMMARY, SAMPLE SELECTION

In this paper, we use protocluster candidates and the galaxy catalog constructed in T18. They draw overdensity maps of g -dropout galaxies from HSC-SSP S16A internal data release, which is a part of PDR1 (Aihara et al. 2018b). Here, we briefly summarize the procedure for the selection of g -dropout galaxies and protocluster candidates.

2.1. Galaxy Selection

T18 use the HSC-SSP S16A internal data release for selecting g -dropout galaxies. HSC is the prime focus camera of the Subaru Telescope (Miyazaki et al. 2018; Komiyama et al. 2018).

The HSC-SSP survey is a wide and deep survey of over 300 nights by the HSC collaboration (Aihara et al. 2018a). The target fields are divided into three layers (Wide, Deep, and UltraDeep), and five broad bands (*grizy*) and three narrow bands are used (for more details on the HSC filter system, see Kawanomoto et al. 2018). The Wide layer has a 5σ limiting magnitude of $i \sim 26$ mag. HSC-SSP data is processed via *hscpipe* (Bosch et al. 2018), which is a modified version of the Legacy Survey of Space and Time software (Jurić et al. 2015; Axelrod et al. 2010; Ivezić et al. 2008). In the S16A data release, the total survey area of the Wide layer observed in all bands and reaching to the full depth is 178 deg^2 , and the average seeing is $0.56''$ in i band and $0.65'' - 0.7''$ in other bands.

T18 construct a g -dropout galaxies sample from the *gri* band photometry. Only five regions in the Wide layer have enough depth (XMM-LSS, WIDE12H, GAMA15H, HECTOMAP, and VVDS) to construct a homogeneous map of the galaxy distribution. T18 impose color criteria (for $g - r$ and $r - i$) and a limiting magnitude cutoff (5σ significance in the i band and 3σ significance in the r band), based on the *Cmodel* magnitudes (Bosch et al. 2018). Various flags are used to select objects with the clean photometry and not affected by cosmic rays and so on (For more detail, see T18).

2.2. Protoncluster Selection

T18 select protocluster candidates according to the peak value of the overdensity significance. The overdensity map of g -dropout galaxies is drawn from their surface number density through the fixed aperture method. This method distributes circular apertures on an every $1'$ grid and estimates the surface number density of galaxies from the number of galaxies inside the apertures. They define the aperture size of $1.8'$, which corresponds to ~ 0.75 physical Mpc at $z \sim 3.8$. This size is the smallest one expected for protoclusters of “Fornax-type” clusters ($M_{\text{halo}} \sim 1 - 3 \times 10^{14} M_\odot$ at $z \sim 0$), as predicted by simulations (Chiang et al. 2013).

T18 only focuses on regions whose limiting 5σ magnitudes for g , r , i band are deeper than 26.0, 25.5, and 25.5 mag, respectively, giving an effective survey area of 121 deg^2 . For drawing the overdensity map, T18 utilizes the g -dropout galaxies that are brighter than 25 mag in i band. T18 select 179 overdense regions whose peak overdensity significance is greater than 4σ as protocluster candidates, following Toshikawa et al. (2016). T18 evaluate that about $\geq 76\%$ of such regions will evolve into halos with a mass greater than $10^{14} M_\odot$ at $z \sim 0$.

This large sample of protoclusters allows T18 to conduct an angular clustering analyses and estimate the mean dark matter halo mass as $\langle M_{\text{halo}} \rangle = 2.3^{+0.5}_{-0.5} \times 10^{13} h^{-1} M_\odot$. According to the extended Press-Schechter model, halos with such a large mass is indeed expected to evolve into those with $\langle M_{\text{halo}} \rangle = 4.1^{+0.7}_{-0.7} \times 10^{14} h^{-1} M_\odot$ at $z \sim 0$.

We have to define the volume of protoclusters in order to measure the UVLF. It should be noted that these protocluster candidates and their members have the redshift uncertainty ($\delta z \sim 1$) since this method is based on the dropout technique. We approximate the shape of protoclusters as cylinders. The cross-section of the cylinder is a circle with a radius of $1.8'$ corresponding to 0.75 physical Mpc, which is the same size as the aperture in the overdensity map. The line-of-sight length is equivalent to the diameter of the cross-section. Therefore, we select protocluster member galaxies from galaxies that are located within a projected $< 1.8'$ from the center of the overdensity peak. We consider a masked region in determining protocluster volumes. Note that we do not consider the particular morphology of each protocluster. For example, some protoclusters, particularly more massive ones, can be bigger (e.g., Muldrew et al. 2015; Chiang et al. 2013). Some studies also argue that the shape of protoclusters can be described in the triaxial model (Lovell et al. 2018). The radius for selecting member galaxies in the study is the minimum size of protoclusters predicted by the simulation (Chiang et al. 2013), thereby our selected regions are expected to

contain pure protocluster members, but we might miss some member galaxies that are located in the outermost regions of protoclusters. As we discuss in Section 5.2, our results for the shape of UVLF do not significantly change even if we change the radius of the cross-section and the depth.

3. REST-UV LUMINOSITY FUNCTION MEASUREMENT

3.1. Formulation of Luminosity Function

We estimate the UV absolute magnitude, which is the absolute magnitude at 1500 Å in the rest-frame from the apparent magnitude. As mentioned in Section 2.2, our protocluster galaxies have a significant redshift uncertainty since they are selected from g -dropout galaxies. Therefore, we fix $\bar{z} = 3.8$ as the typical redshift. We convert the i band magnitude (m_i) by using the following equation;

$$M_{UV} = m_i + 2.5 \log(1 + \bar{z}) - 5 \log\left(\frac{d_L(\bar{z})}{10 \text{ pc}}\right) + (m_{1500(1+\lambda)} - m_i) \quad (1)$$

Here, $d_L(\bar{z})$ is the luminosity distance at $z = \bar{z}$ in the unit of pc. We assume that the g -dropout galaxies' SED at rest-UV is flat in f_ν , which leads to a k -correction factor ($m_{1500(1+\lambda)} - m_i$) of zero, following Ono et al. (2018).

We measure only the projected number density from the photometric data; therefore, our protocluster galaxy sample has some possible contaminants. One is fore/background g -dropout galaxies outside the protocluster regions, hereafter called “field galaxies”. The effective redshift range of g -dropout galaxies is significantly larger than the protocluster's transverse size, so we must subtract the contribution of field galaxies from the measured surface number density in protocluster regions. The number density of field galaxies can be approximated by the UVLF of field galaxies (field UVLF) since the volume fraction of protocluster is small compared to the total survey volume. In addition to field galaxies, g -dropout galaxies themselves may inevitably have some contaminants such as stars and low-redshift galaxies due to the color selection uncertainties, which should be removed from the sample. These objects can be assumed to be homogeneously distributed if we combine all protoclusters, which are separated on the whole sky; therefore, their contamination rate should be the same both inside and outside of the protocluster regions. This implies that the subtraction of the field UVLF without the contamination correction provides a clean estimate of the number density of protocluster galaxies.

One possible contamination source that is hard to assume to distribute homogeneously is low- z galaxy clusters at $0.3 < z < 0.6$, where Balmer breaks are hardly distinguishable from Lyman break at $z \sim 4$. Oguri et al. (2018) construct a galaxy cluster sample at $0.1 < z < 1.1$ from 232 deg² HSC-SSP data. They find 620 clusters at $0.3 < z < 0.6$, implying their surface number density as 2.67 deg⁻². The possibility that our protoclusters are overlapped with galaxy clusters at $0.3 < z < 0.6$ within 1.8' (i.e., protocluster size) is only 0.59%. Therefore, we conclude that all contamination is negligible to estimate the the UVLF of protocluster galaxies (PC UVLF).

We correct the effective volume of g -dropout galaxies to the protocluster effective volume by a factor F defined as;

$$F(M_{UV}) = \frac{\langle C(M_{UV}, z) \frac{dV(z)}{dz} \delta z \rangle}{V_{\text{eff}}(M_{UV})} \quad (2)$$

Here, $C(M_{UV}, z)$ is the completeness function of the g -dropout selection estimated in Section 3.2. δz is the redshift interval that corresponds to the depth of the cylinder volume of protoclusters (see Section 2.2). $dV(z)/dz$ is the differential comoving volume. The $V_{\text{eff}}(M_{UV})$ is the effective volume for g -dropout galaxies in 1.8' aperture, which is defined as follows (e.g., Hogg 1999);

$$V_{\text{eff}}(M_{UV}) = \int C(M_{UV}, z) \frac{dV(z)}{dz} dz \quad (3)$$

The numerator of $F(M_{UV})$ corresponds to the effective volume of a protocluster, whose shape is defined in Section 2.2. Therefore, $F(M_{UV})$ is the ratio of the effective volume of the protoclusters and the effective volume of the redshift range of the entire g -dropout selection. Since we do not know the exact redshifts of each system, we use the average numerator weighted by the redshift selection function (i.e., the completeness function).

Then, the PC UVLF is described as follows,

$$\Phi_{\text{PC}}(M_{UV}) = \frac{1}{F(M_{UV})} \left(\frac{n_{\text{obs,PC}}(M_{UV})}{V_{\text{eff}}(M_{UV})} - \Phi_{\text{field}}(M_{UV}) \right) \quad (4)$$

where $n_{\text{obs,PC}}(M_{UV})$ is the observed number of g -dropout galaxies in protocluster regions defined in Section 2.2 in each magnitude bin. $\Phi_{\text{field}}(M_{UV})$ is the field UVLF without the contamination correction (see Section 3.3). In order to determine $\Phi_{\text{PC}}(M_{UV})$, we estimate the completeness function of g -dropout galaxies $C(M_{UV}, z)$ and the field UVLF without contamination treatment in the following section.

3.2. Completeness Estimation

As in the previous studies of UVLFs of field LBGs (e.g., Ono et al. 2018; van der Burg et al. 2010; Yoshida

et al. 2006), we insert mock galaxies into actual images and estimate a completeness function. This is derived as a function of the redshift and the magnitude.

Mock galaxies are inserted into the coadd images of the g, r, i band images of HSC-SSP products. We generate mock images through the `Balrog`¹ (Suchyta et al. 2016), which inserts mock galaxies with the help of the `galsim`² (Rowe et al. 2015) followed by their detection and measurement through `SourceExtractor`. However, the HSC-SSP source catalog is constructed based on `hscpipe`; therefore, we detect and measure the photometry of the mock galaxies through `hscpipe`, instead. We use `hscpipe` version 4, which is the same software used for the HSC-SSP S16A data release.

We assume that the surface brightness profile follows the Sérsic profile (Sérsic 1963) with a fixed Sérsic index of 1.5 for mock galaxies. In addition, the effective size distribution is assumed to be consistent with that of Shibuya et al. (2015). The real profile of mock galaxies are considered with the point spread function (PSF) of that field by convolving it taken from `PSFEx`³ (Bertin 2011). The SED of mock galaxies are generated using the `CIGALE`⁴ (Boquien et al. 2019). We assume a constant star formation and use the single stellar population models of Bruzual & Charlot (2003). We adopt the Salpeter initial mass function (IMF) (Salpeter 1955) with an age of 100 Myr and metallicity of $Z/Z_{\odot} = 0.2$. The dust extinction follows Calzetti et al. (2000) with $E(B - V) = 0.0 - 0.4$ mag. The IGM absorption is accounted for according to Meiksin (2006). We change their redshift from 3.0 to 5.0 with interval of $\delta z \sim 0.1$.

Due to the slight differences in depths among the five fields, we estimate the completeness function for each field. We select one region called `tract`, with an area of 2.3 deg^2 , for each field to execute the procedure. The number of inserted galaxies is about 35 per arcmin^2 . From the detected catalogs, we select mock g -dropout galaxies by the same criteria as used in T18, including color, magnitude, and flags selection.

For each field, we calculate the completeness as the number ratio of selected mock g -dropout galaxies to all inserted objects in each magnitude and redshift bin. Figure 1 shows the completeness function of each field, demonstrating that five fields have almost the same completeness.

3.3. Luminosity Function of Field Galaxies Without Contamination Treatment

From the completeness function and Equation 5 below, we estimate the field UVLF without contamination treatment.

$$\Phi_{\text{field}}(M_{\text{UV}}) = \frac{n_{\text{obs,field}}(M_{\text{UV}})}{V_{\text{eff}}(M_{\text{UV}})} \quad (5)$$

Here, $n_{\text{obs,field}}(M)$ is the observed number of field galaxies and contaminants of $M_{\text{UV}} = M$. Before deriving $n_{\text{obs,field}}(M)$, we remove all known low- z galaxies, stars, or QSOs from the available spectroscopic survey archives, such as SDSS DR12 (Alam et al. 2015), HectoMAP cluster survey (Sohn et al. 2018), and VIPERS DR1 (Garilli et al. 2014). The majority of matched objects are galaxies at $0.3 < z < 0.6$ and QSOs at the same redshift distribution of g -dropout galaxies. Only two QSOs, which overlap with the protocluster region, are removed from the sample (Uchiyama et al. 2018).

We compare the input total magnitude and the measured $2.0''$ aperture magnitude of mock galaxies used in Section 3.2, and find that $2.0''$ aperture magnitude has a $+0.08$ mag offset on average from the input magnitude. Therefore we apply a 0.08 mag aperture correction to our measured $2.0''$ magnitudes to derive the total magnitudes. We confirm that the derived total magnitudes are consistent with measured aperture magnitudes with the larger apertures, such as $3.0''$, $4.0''$. We also correct the galactic extinction by using the extinction map from Schlegel et al. (1998).

This UVLF is not necessarily the same as the field UVLF derived in previous studies (e.g., Ono et al. 2018; Bouwens et al. 2015) since our function includes contaminants, as seen in Figure 2. We derive the field UVLFs for each field.

The bottom panel of Figure 2 shows the difference between the average of the UVLFs and that of Ono et al. (2018) normalized by this UVLF. Since the UVLF of Ono et al. (2018) exclude contaminants, this represents the expected fraction of contaminants among our g -dropout galaxies. We can find that this ratio is consistent with that in Ono et al. (2018), overplotted in the bottom panel of Figure 2. We conclude that our completeness function is consistent with previous studies. Hereafter, we will use these UVLFs and the completeness function to estimate the PC UVLF.

3.4. Protocluster Luminosity Function

Here, we estimate the PC UVLF according to Equation 4. Two protoclusters are excluded since they are located in low-quality regions with quite shallow limiting magnitudes ($m \sim 25.6$ mag for 5σ i -band limiting mag-

¹ <https://github.com/emhuff/Balrog>

² <https://github.com/GalSim-developers/GalSim>

³ <https://www.astromatic.net/software/psfex>

⁴ <https://cigale.lam.fr/>

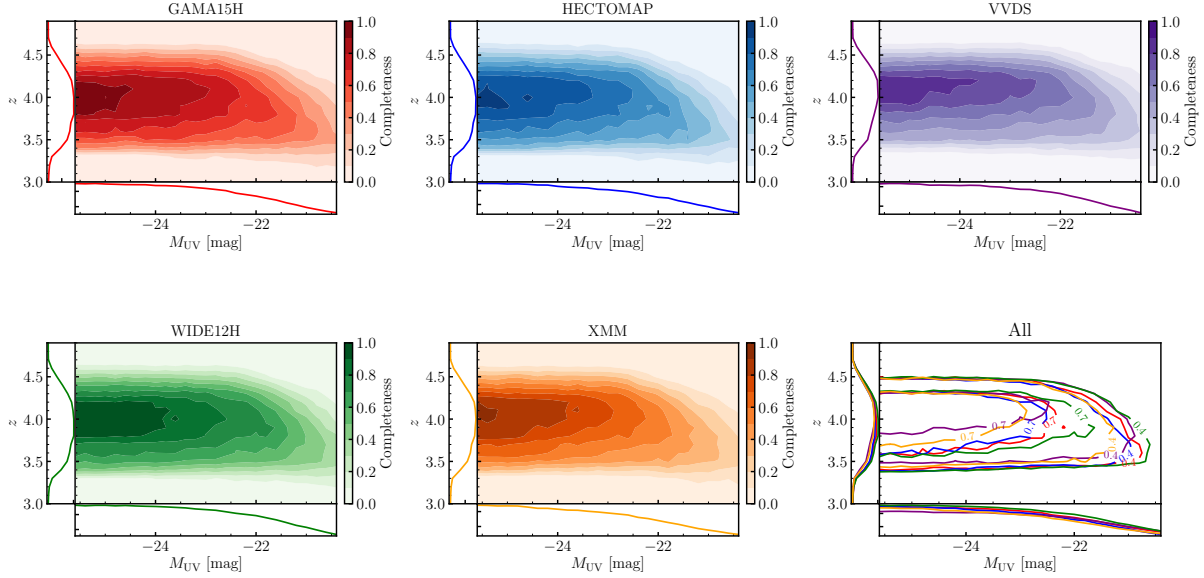


Figure 1. Completeness functions for each target field. The bottom right panel shows their comparison. Colors match those shown in each panel of single field. Values written in the contour in the right bottom panel represent the completeness.

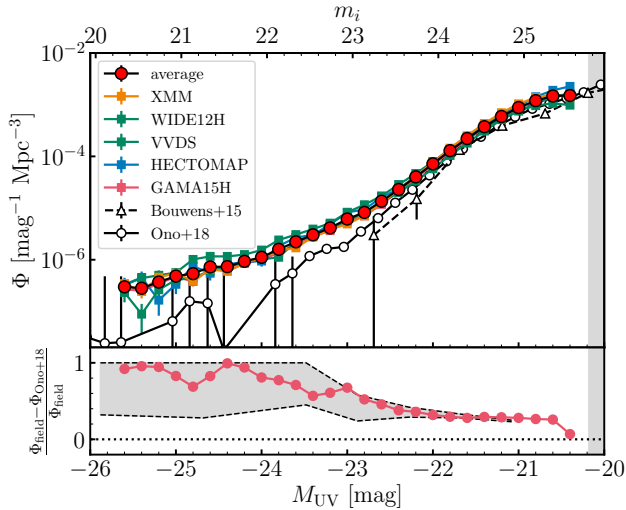


Figure 2. Top panel: The field UVLF at $z \sim 4$ for each field (squares) and their average (red circles). Black open circles and triangles are UVLFs in the literature (Ono et al. 2018; Bouwens et al. 2015). Note that we do not correct for contaminants. Bottom panel: The red circles show the difference between the average of this work UVLFs, which is not corrected for contaminants, and the UVLF from Ono et al. (2018) normalized by this work’s UVLF. Gray shaded region shows the contamination rate of g -dropout galaxies estimated in Ono et al. (2018). The red circles correspond to a contamination fraction of our g -dropout galaxies, which is in good agreement with that in Ono et al. (2018).

nitude); thus 177 protocluster regions are used for estimating the PC UVLF. Since the completeness function and $\Phi_{\text{field}}(M_{\text{UV}})$ have been determined for each field, the PC UVLF is also estimated for each field separately,

and we take the average weighted by the total area for each field as our final PC UVLF. We note that all PC UVLF for each field are overall consistent within the uncertainty.

We show the average PC UVLF of the HSC-SSP protocluster candidates in Figure 3. Our PC UVLF has apparent discrepancies with the field UVLF in the literature (e.g., Ono et al. 2018). First, the amplitude is much higher than the field UVLF, with the integrated value of the PC UVLF at $M_{\text{UV}} \leq -20.3$ is about 230 times higher than that of the field UVLF of Ono et al. (2018). Second, its shape is remarkably different from the field UVLF. The amplitude-matched field UVLF is also shown in the top panel of Figure 3 for reference, and compared with that, the PC UVLF has a significant excess towards the bright-end ($M_{\text{UV}} \leq -20.8$). The trend can also be seen on the bottom panel of Figure 3, which shows the ratio of the PC and the field UVLF. We see that the excess gets larger towards the brighter bin. If the shapes are identical between them, this ratio should stay constant at any brightness.

Since the number density of galaxies decreases towards the bright-end, so the photometric error of each galaxy might enhance the amplitude of the bright-end of UVLF, which is known as “Eddington Bias” (Eddington 1913). We estimate the effect of this bias by convolving the error distribution of magnitude to the field UVLF of Ono et al. (2018). The detail of this analysis is described in Appendix A. We confirm that the Eddington bias is not significant to generate the shape of our PC UVLF.

Since contributions from low- z contaminants, which distribute homogeneously, are statistically subtracted

from the sample as mentioned in Section 3.1, the bright-end excess is not due to low- z galaxy contaminants. Also, the PC UVLF may depend on $F(M_{\text{UV}})$, which is the ratio of the effective volume of protoclusters and g -dropout galaxies. We confirm that the bright-end excess of PC UVLF does not change even if we fix $F(M_{\text{UV}}) = 1$, as seen in Appendix B.

The rest-UV luminosity of galaxies represents their SFR. Therefore, this result indicates that overdense regions at $z \sim 4$ have not only a high SFRD caused by the excess of the number of galaxies, but also a higher fraction of galaxies with high SFR compared to those in the blank field. This trend is also seen in some protoclusters at lower redshifts. For example, Shimakawa et al. (2018) estimate the SFR of HAEs in a protocluster at $z = 2.5$, and they also find that HAEs in the densest regions tend to have a higher SFR than those in the outskirts. Koyama et al. (2013) report a similar trend from HAEs in protoclusters at $z \sim 2$. This paper, for the first time, shows that the enhancement of star formation of UV-bright galaxies in overdense regions can already be seen as early as from $z \sim 4$. We have to note that some bright ($M_{\text{UV}} < -23.0$) LBGs can be AGNs, whose UV emission cannot be a proxy of SFR of their host galaxies (e.g., Adams et al. 2019; Ono et al. 2018). We discuss a possible contribution from AGN in Section 5.3.

3.5. Function Fitting

To compare the shape of the PC UVLF with the field UVLF more quantitatively, we fit the Schechter function (Schechter & Press 1976), which is defined as follows;

$$\phi(L)dL = \phi^* \left(\frac{L}{L^*}\right)^\alpha \exp\left(-\frac{L}{L^*}\right) d\left(\frac{L}{L^*}\right) \quad (6)$$

where α is the faint-end slope, L^* is the characteristic luminosity, and ϕ^* is the overall normalization. This function can be also expressed as a function of the absolute magnitude M_{UV} ,

$$\Phi(M_{\text{UV}}) = \frac{\ln 10}{2.5} \phi^* 10^{-0.4(M_{\text{UV}} - M_{\text{UV}}^*)(\alpha+1)} \times \exp(-10^{-0.4(M_{\text{UV}} - M_{\text{UV}}^*)}) \quad (7)$$

We fit the Schechter function in terms of absolute magnitude to the PC UVLF using the χ^2 minimization method. We show the best-fit Schechter function in Figure 4 and the parameters in Table 1. Compared to the best-fit parameters of the field UVLF in previous studies (Ono et al. 2018; Bouwens et al. 2015; van der Burg et al. 2010; Yoshida et al. 2006), our PC UVLF has a less steep faint-end slope, as shown in Figure 5. Our best-fit M_{UV}^* is consistent with that of the field UVLFs at the 68/95% confidence level. This implies that the

PC UVLF has a different shape compared to the field UVLF, although the discrepancy between our PC UVLF and the best-fit Schechter function is large, particularly at the bright-end ($M_{\text{UV}} < -23$).

The large reduced χ^2 shown in Table 1 implies this failure of fitting at the bright-end. This can be because the PC UVLF does not seem to have a clear exponential decrease at the bright-end. Therefore, we try to fit another functional form. Recent UVLF studies of field galaxies at higher redshift ($z \geq 4$) have suggested that the galaxy UVLF can be well described by a double power-law (DPL) function (e.g., Bowler et al. 2019, 2015; Ono et al. 2018). The DPL function is defined as follows;

$$\phi(L)dL = \phi^* \left[\left(\frac{L}{L^*}\right)^{-\alpha} + \left(\frac{L}{L^*}\right)^{-\beta} \right]^{-1} \frac{dL}{L^*} \quad (8)$$

,where β represents the power-law slope at the bright-end ($M_{\text{UV}} < M_{\text{UV}}^*$). We fit this function in terms of absolute magnitude, also. We fix the faint-end slope α to be the same as that of the best-fit Schechter function. We also show the best-fit DPL function in Figure 4, and their parameters in Table 1. The DPL function fits better than the Schechter function, even though the best-fit DPL function still has some deviation from the observed PC UVLF at $M_{\text{UV}} < 23$.

The excess from the best-fit Schechter/DPL function of UVLFs of field galaxies is often explained by AGNs. Ono et al. (2018) claim that the gap of UVLFs of field galaxies from their best-fit Schechter function at $z \sim 4 - 7$ is explained by the contribution of AGN UVLFs at the same redshift. Also, Konno et al. (2016) construct the Ly α luminosity function of LAEs at $z = 2.2$ and argue that the gap at the brightest-end from its best-fit is due to AGNs. We discuss the possible contribution from AGNs in Section 5.3 and do not reject the possibility of the gap in both best-fit results due to AGNs. However, we can not conclude which functions represent the galaxy UVLF more precisely. Therefore, we use both fitting functions in the following sections.

4. IMPLICATIONS FROM THE PROTOCLUSTER GALAXY LUMINOSITY FUNCTION

4.1. Stellar Mass Function

We estimate the SMF based on the measured PC UVLF, assuming that all protocluster g -dropout galaxies are located on the star formation main-sequence of field galaxies at the same redshift. We utilize the main-sequence estimated by Song et al. (2016), which determine the main-sequence by applying SED-fitting analysis to field photo- z selected galaxies from Finkelstein

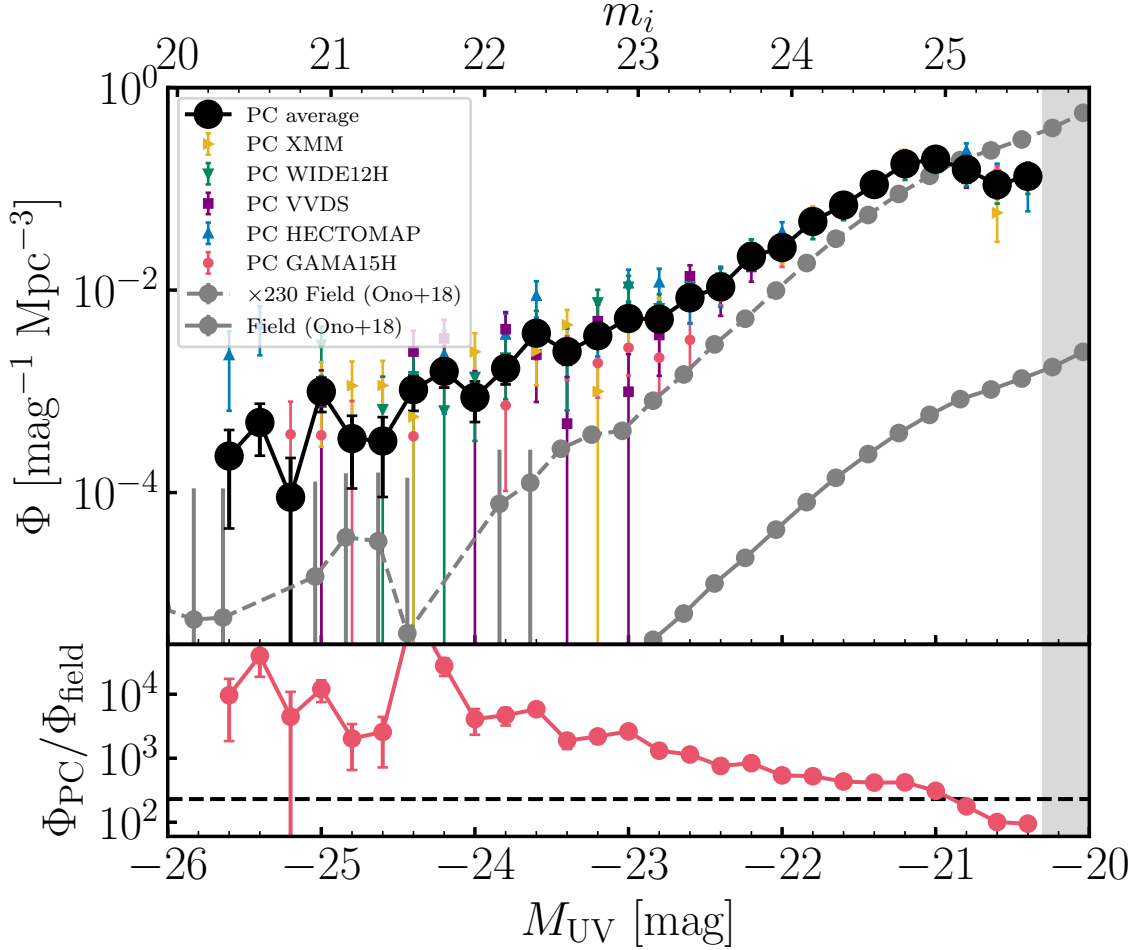


Figure 3. The luminosity function of galaxies in protocluster candidates at $z \sim 4$. The color-coded markers represent the PC UVLF for each survey field. The black circles show the average of all fields. For reference, we show the field UVLF of Ono et al. (2018) (gray solid line with circles) and shifted upward to match the PC UVLF (gray dashed line with circles). The bottom panel shows the ratio of the PC UVLF and the field UVLF (red circles). The black dashed line shows the value of the ratio of the sum of each UVLF. For both panels, the magnitude range that is fainter than the depth is shaded in gray.

M_{UV}^* (mag)	ϕ^* (Mpc^{-3})	α	β	χ^2_ν
Schechter function				
$-20.61^{+0.12}_{-0.14}$	$0.48^{+0.02}_{-0.02}$	$-0.16^{+0.25}_{-0.25}$	-	11.2
Double power-law function				
$-21.13^{+0.04}_{-0.04}$	$0.31^{+0.01}_{-0.01}$	(-0.16)	$-3.59^{+0.08}_{-0.11}$	5.5

Table 1. The best-fit parameters and the reduced χ^2 of the Schechter and DPL functions fitted to the PC UVLF. We fix the faint-end slope in the case of the DPL to the best-fit value in the case of the Schechter function.

et al. (2015). We assume the main sequence is equivalent between protoclusters and the field, which is supported by observational studies (e.g., Long et al. 2020; Shi et al. 2019a; Koyama et al. 2013) and a theoretical study (e.g., Lovell et al. 2020), while some studies report a large contribution from star burst galaxies in protoclusters (e.g.,

Miller et al. 2018), leading to the possibility of different main sequence from that of field galaxies.

We use the “constant-scatter galaxy SMF” method, which is conducted in some previous studies (e.g., Song et al. 2016). First, M_{UV} is randomly assigned. Its probability distribution for each M_{UV} is approximated by the PC UVLF, in which Gaussian random errors for each bin are assigned, whose 1σ is equivalent to that of the observed PC UVLF. The M_{UV} is converted into the stellar mass M_* according to the M_* - M_{UV} relation of Song et al. (2016) with a constant scatter of 0.4 dex, and finally, the stellar mass distribution is obtained. This procedure is repeated for 1000 times, and the SMF of protocluster galaxies (PC SMF) is obtained by taking their average. The uncertainty of the SMF is taken from the variation among 1000 results. The SMF of field galaxies (field SMF) is also estimated from the field UVLF of Ono et al. (2018) in the same manner. We find

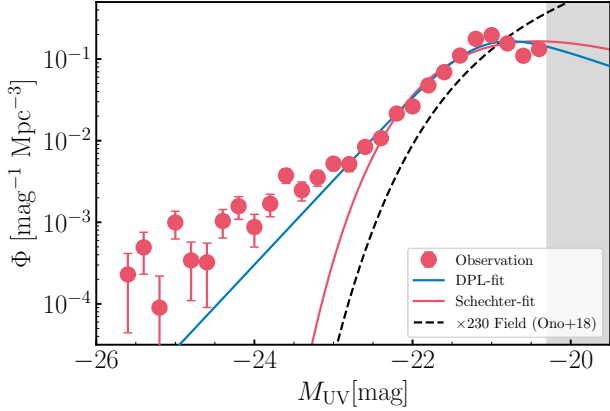


Figure 4. The result of the fitting of the Schechter/DPL function to PC UVLF. Circles show the derived PC UVLF. The red (blue) lines represent the best-fit of the Schechter (DPL) function. As a reference, the black dashed line is the best-fit Schechter function of the field UVLF in Ono et al. (2018). Same as Figure 3, the gray shade represents the magnitude range which is not discussed.

that the estimation of SMFs has only a negligible change within the uncertainty when we use the main sequence of Tomczak et al. (2016), which has a flatter massive end ($\log(M_*/M_\odot) > 10.5$), compared to the main sequence of Song et al. (2016) as shown in Figure 6.

Figure 6 shows our SMF estimate. We normalize them to fix the value at $\log(M_*/M_\odot) = 10$ for the easy comparison. The gray shaded region ($\log(M_*/M_\odot) < 9.72$) in Figure 6 shows the incomplete mass range due to the limiting magnitude ($M_{UV} > -20.3$). We hereafter discuss the SMF in the stellar mass range of $\log(M_*/M_\odot) > 9.72$. The PC SMF shows a clear excess from that of field galaxies towards the massive end, suggesting that protoclusters contain a relatively high fraction of massive galaxies compared to the field. Here, we mention three notes. First, this SMF only includes g -dropout galaxies, which are typically star-forming, and we do not consider quiescent galaxies. Recent studies report the existence of massive quiescent galaxies even at $z \sim 4$ in the blank field (e.g., Valentino et al. 2020; Tanaka et al. 2019), but the fraction of them are expected to be small ($< 5\%$) according to field SMFs (e.g., Davidzon et al. 2017), though the value in overdense environments has uncertainty. Therefore, we ignore the effect of quiescent galaxies. Second, the bend of the PC UVLF around $M_{UV} < -23$ is not seen in PC SMF. This is because the SMF is estimated from the main-sequence with the constant scatter, which is so called “Eddington Bias”. Third, the most massive-end ($\log(M_*/M_\odot) > 11.15$) is dominated by objects with $M_{UV} \leq -23$. As we mention in Section 5.2, objects in

such magnitude range can be AGNs; therefore, values of the SMF in this mass range can have uncertainty.

We fit the Schechter function to the measured PC SMF as well as to the field SMF at $z \sim 4$. We can see that the PC SMF has a higher characteristic stellar mass and faint-end slope than the field SMF as seen in Figure 7. Protocluster galaxies have about 2.8 times higher characteristic stellar mass than field galaxies. This also supports the result that protocluster galaxies are more massive than field galaxies.

The difference of the PC SMF and the field SMF is also seen in simulations at $z \sim 4$ (Lovell et al. 2018; Muldrew et al. 2015). In Figure 6, we compare our PC SMF and the field SMF with those predicted in Lovell et al. (2018). Lovell et al. (2018) use the semi-analytical model (SAM) from Henriques et al. (2015) and trace the evolutionary track of halos with $M_{200}/M_\odot > 10^{14}$ at $z \sim 0$ to higher redshift. M_{200} is the mass within $r < r_{200}$, where the density is 200 times the critical density. We use their predicted SMFs constructed from galaxies with $\text{SFR} > 5 M_\odot \text{ yr}^{-1}$ at $z = 3.10$ and 3.95 . The average redshift of our protocluster sample is between redshifts of these predicted SMFs. Our SMF is found to be almost consistent with the theoretical predictions and located between the predicted SMF at $z = 3.95$ and that at $z = 3.10$. Though the PC SMF has higher amplitude than the theoretical prediction at the most massive-end ($\log(M_*/M_\odot) > 11.15$), this can be explained by the contribution of AGNs mentioned above.

We compare our PC SMF with those of (proto)cluster galaxies at lower redshifts. Shimakawa et al. (2018) estimate a SMF of HAEs in a protocluster called USS1558-003 at $z \sim 2.5$. Nantais et al. (2016) focus on four galaxy clusters at $z \sim 1.5$ from the Spitzer Adaptation of the Red-sequence Cluster Survey (SpARCS) (Muzzin et al. 2009; Wilson et al. 2009; Demarco et al. 2010). van der Burg et al. (2013) present a SMF of galaxies of ten rich clusters in the Gemini Cluster Astrophysics Spectroscopic Survey (GCLASS) at $0.86 < z < 1.34$. The SMF of galaxies in 21 clusters detected with the Planck satellite at $0.5 < z < 0.7$ is also presented in van der Burg et al. (2018). Calvi et al. (2013) estimate a SMF of cluster galaxies from the Wide-field Nearby Galaxy-cluster Survey (WINGS) at $0.04 \leq z \leq 0.07$ (Fasano et al. 2006), and compare with that of field galaxies at the same redshift. Figure 8 shows our PC SMF with other SMFs and the field SMF. Same as in Figure 6, we normalize the amplitude of all SMFs at $\log(M_*/M_\odot) = 10$. This is because the definition of the (proto)clusters’ volume depends on studies, leading to the difficulty of the amplitude comparison. Therefore, we only focus on the shape difference of these SMFs. We

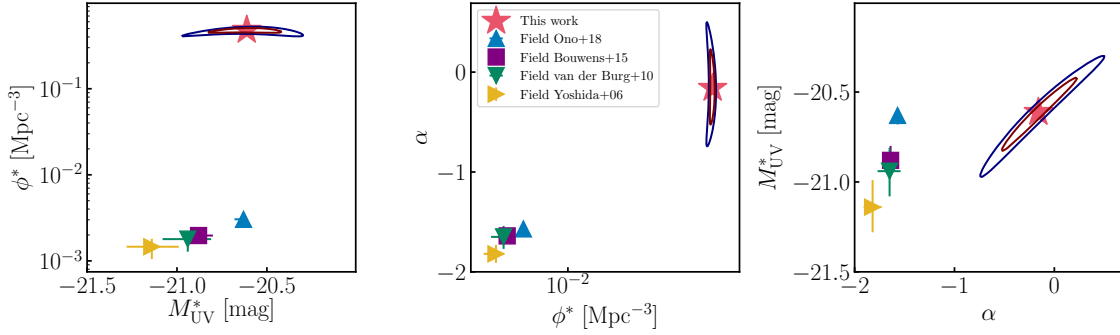


Figure 5. The comparison of best-fit parameters of our PC UVLF with those of the field UVLFs from the literature. Red stars represent this work, and blue, purple, green and yellow markers represent Ono et al. (2018), Bouwens et al. (2015), van der Burg et al. (2010), and Yoshida et al. (2006), respectively. Red and Blue contours represent the 68.3%, and 95.5% confidence levels of the best-fit parameters of our PC UVLF, respectively.

also convert their assumed IMF to Salpeter IMF, which is used in Song et al. (2016).

We can see that there is a dearth of massive galaxies in the SMF of our protoclusters at $z \sim 4$ compared to those at lower- z . This suggests that our protoclusters at $z \sim 4$ are still in the process of mass growth. Particularly, from $z \sim 4$ (HSC-SSP protoclusters) to $z \sim 1$ (van der Burg et al. 2013), SMFs shows a monotonic growth at the massive end. At $z \sim 0-1$, the ratio of SMFs at massive-end to that at low mass-end decreases towards lower redshift. This may be due to the significant contribution of less massive infalling galaxies. We discuss it in more detail in Section 5.4.

We note that these SMFs are based on galaxy clusters selected by different methods. They might be at different stages of the evolution of clusters (Toshikawa et al. 2020), which may make it difficult to compare them with each other. Moreover, protocluster sample of this study and Shimakawa et al. (2018) only focus on star-forming galaxies, while others contain quiescent galaxies. The fraction of quiescent galaxies at $z > 2$ is known to be smaller than that at lower redshift, so we ignore the effects of this difference. Also as mentioned in Section 2.1, our protocluster candidates are overdense regions expected to evolve into clusters with $\langle M_{\text{halo}} \rangle = 4.1^{+0.7}_{-0.7} \times 10^{14} h^{-1} M_{\odot}$ at $z \sim 0$. The majority of clusters from WINGS is as massive as $M_{200} \sim (1-10) \times 10^{14} M_{\odot}$ (Biviano et al. 2017), which is same mass range as the expected halo mass of our protoclusters. On the other hand, the cluster halo mass of other studies is $M_{200} \sim 3 \times 10^{14} M_{\odot}$ for SpARCS (Lidman et al. 2012) and GCLASS (van der Burg et al. 2013), and $M_{200} \sim (3-13) \times 10^{14} M_{\odot}$ in van der Burg et al. (2018). These clusters are already as massive as WINGS clusters, even at $z \sim 1$, so they may grow more by $z \sim 0$, leading them to have difficulty for comparing with WINGS clusters and our sample. In addition, the

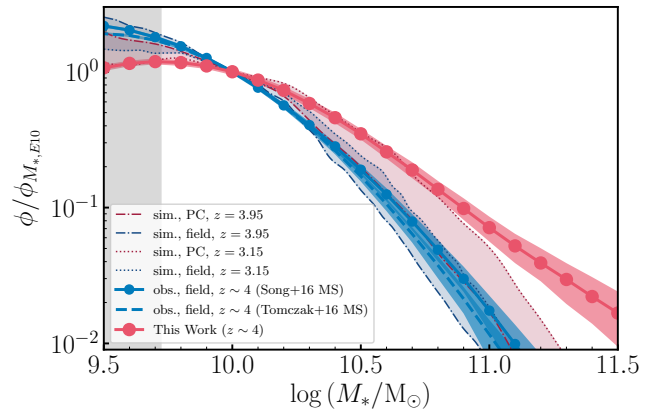


Figure 6. The comparison between our SMFs and SMFs predicted in Lovell et al. (2018). Red and blue circles are SMFs of protocluster and field galaxies estimated in this study. Their 1σ uncertainty are shown in shaded regions with each color. Blue dashed line is the SMF of field galaxies from Tomczak et al. (2016). Red and blue dash-dotted (dotted) lines are predicted SMFs of galaxies in protocluster and those in the field at $z=3.95$ ($z=3.10$), respectively. We normalize SMFs at $\log(M_*/M_{\odot}) = 10.0$.

halo mass of USS1558-003 is not estimated; therefore, it is still under debate whether HSC-SSP protoclusters at $z \sim 4$ are progenitors of protoclusters such as USS1558-003.

4.2. The Diversity of Protocluster Luminosity Functions

Our protocluster sample has some variation in terms of overdensity. As shown in Figure 1 of Uchiyama et al. (2018), the overdensity of protoclusters ranges from 4σ to 9.5σ , and overdensity and descendant halo mass are broadly positively correlated (Toshikawa et al. 2016). Here, we make subsamples of protoclusters according to the overdensity and construct UVLFs for each subsample.

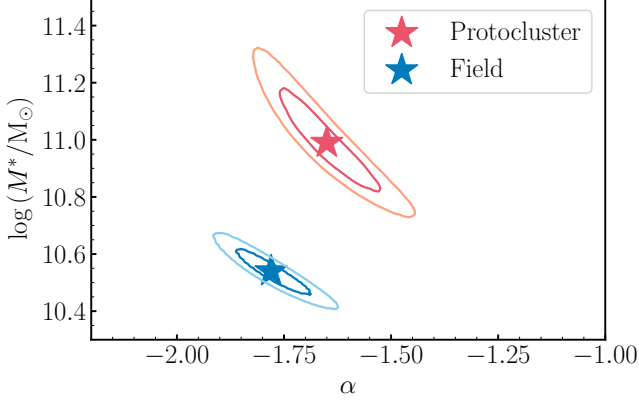


Figure 7. The best-fit parameters of the Schechter function to the PC SMF (Red star) and the field SMF (Blue star). The contours represent their 68/95% confidence interval.

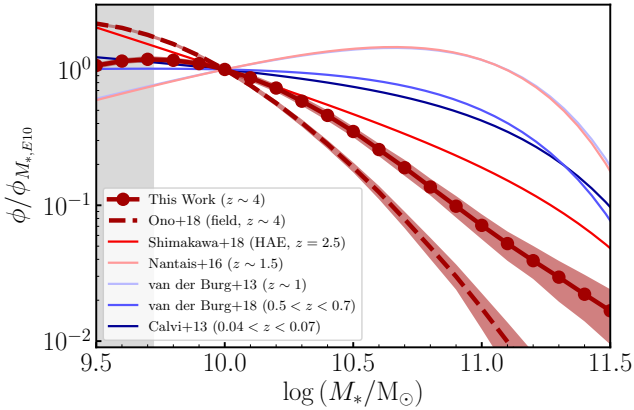


Figure 8. SMFs of (proto)cluster galaxies at different redshift. Their amplitudes are normalized at $\log(M_*/M_\odot) = 10.0$. A red line with circles show that of protocluster galaxies at $z \sim 4$ (this work). For reference, the SMF of field galaxies estimated from the field UVLF of Ono et al. (2018) is plotted in a red dashed line. Their shaded region shows the 1σ uncertainty of them. Other red lines show SMFs of $z \geq 1.5$ (proto)clusters from other studies (Shimakawa et al. 2018; Nantais et al. 2016), and blue lines show SMFs of $z \leq 1$ clusters (van der Burg et al. 2013, 2018; Calvi et al. 2013).

We divide protocluster samples into four groups according to their overdensity δ : 1). $4\sigma \leq \delta < 5\sigma$, 2). $5\sigma \leq \delta < 6\sigma$, 3). $6\sigma \leq \delta < 7\sigma$, 4). $7\sigma \leq \delta$. The numbers of protoclusters in each subgroup are 120, 37, 13, and 7, respectively. In Figure 9, we show the PC UVLF for each subsample. The amplitude of the faint-end ($M_{UV} > -21.2$) is almost the same among subsamples, while the bright-end ($M_{UV} < -21.2$) depends on the overdensity of protoclusters. More overdense protoclusters tend to have a higher bright-end amplitude compared to less massive protoclusters. These proto-

clusters can be more spatially extended, which could cause such a dependency on overdensity; however, we find that this is unlikely as discussed in Section 5.2.

The dependency of the bright-end excess on overdensity can be seen even for each protocluster separately. Figure 10 shows the cumulative UVLF of galaxies in each protocluster. The bright-end amplitude of more overdense protoclusters tends to be higher than those of less massive protoclusters, suggesting that protoclusters with higher overdensity significance have brighter objects. More interestingly, almost all of protoclusters at $z \sim 4$ have this excess at the bright-end compared to those of field galaxies, although the variation is seen even if we focus on only protoclusters with the same overdensity. Therefore, we conclude that the bright-end excess is ubiquitously seen for protoclusters at $z \sim 4$.

In Ito et al. (2019), we investigate the significantly UV-brightest galaxies (proto-BCGs) in this protocluster sample. We find that galaxies in protoclusters containing proto-BCGs are brighter than other protocluster galaxies. This can be due to the overdensity dependence of the bright-end excess since the average overdensity of protocluster containing proto-BCGs is slightly higher ($(5.068 \pm 0.149)\sigma$) than that of all protoclusters ($(4.767 \pm 0.069)\sigma$). To reach the cause of the bright-end excess, we divide a subgroup, which is made in this subsection, into two according to whether protoclusters contain proto-BCGs. At a fixed overdensity, the UVLF of members of protoclusters containing proto-BCGs has the same bright-end amplitude to those of protocluster not containing proto-BCGs. Brighter galaxies of protoclusters containing proto-BCGs are thus due to their higher overdensity.

4.3. Star Formation Rate Density

We estimate the SFRD of protocluster galaxies, based on a combination of the PC UVLF and the far IR (FIR) luminosity density. The PC UVLF is approximated by the best-fit Schechter/DPL function. Parameter spaces with a 68% confidence level estimated in Section 3.5 are employed for the PC UVLF.

We first estimate the UV luminosity density ρ_{UV} from the PC UVLF as $\rho_{UV} = \int_{L_{faint}}^{L_{bright}} L_{UV} \phi(L_{UV}) dL_{UV}$. We set $L_{faint} = 2.7 \times 10^{27} \text{ erg s}^{-1} \text{ Hz}^{-1}$, corresponding to $M_{UV} = -17$ mag, which is the same as applied in Bouwens et al. (2015), and $L_{bright} = 1.1 \times 10^{31} \text{ erg s}^{-1} \text{ Hz}^{-1}$, corresponding to $M_{UV} = -26$ mag.

The FIR ($8 - 1000 \mu\text{m}$) luminosity density ρ_{FIR} is estimated as $\rho_{FIR} = \int_{L_{faint}}^{L_{bright}} L_{FIR} \phi(L_{UV}) dL_{UV}$ with the use of the IRX- β - M_* relation of $z \sim 3$ LBGs (Álvarez-Márquez et al. 2019). The $\beta - M_{UV}$ relation is known to exist even in protocluster galaxies at $z \sim 4$ (Overzier

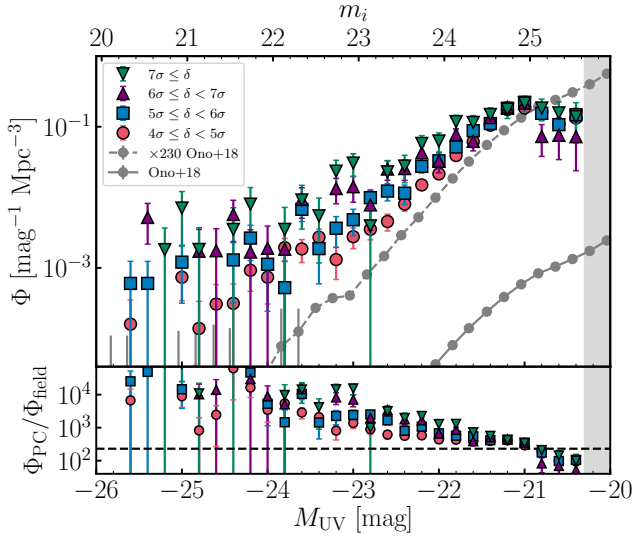


Figure 9. The UVLFs of members of protoclusters grouped according to their overdensities. Red, blue, purple, and green markers show those whose host protoclusters' overdensity are $4\sigma \leq \delta < 5\sigma$, $5\sigma \leq \delta < 6\sigma$, $6\sigma \leq \delta < 7\sigma$, $7\sigma \leq \delta$, respectively. The gray lines are same as in Figure 3.

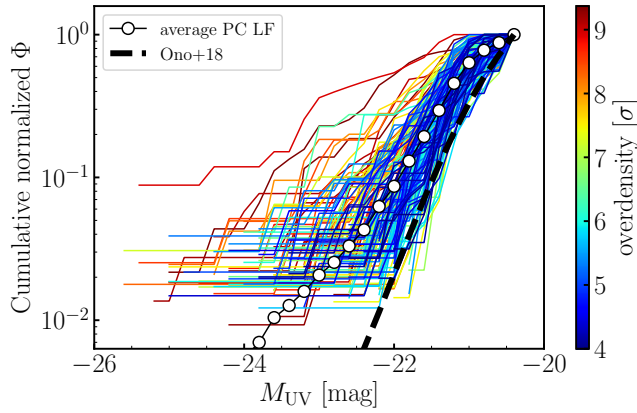


Figure 10. The cumulative UVLFs of galaxies in each protocluster candidate. Colors represent their overdensity significance. For reference, the average cumulative luminosity function of protocluster galaxies (black open circles) and the cumulative luminosity function of field galaxies (dashed line) are also plotted.

et al. 2008). The β distribution is determined by using the conversion equation from $i - y$ color to β in Bouwens et al. (2012). We linearly fit the median value of β distribution in each 0.2 mag magnitude bin of $M_{UV} \leq -20.3$. We use its best-fit parameters with their 1σ error for $\beta - M_{UV}$ relation. We also estimate the $\beta - M_{UV}$ relation of our field galaxies in the same manner and compare it with the literature in Appendix C. Our estimation is consistent with literature within the uncertainty, suggesting that our measurement and the sample selection

is robust. The stellar mass M_* is estimated from the UV absolute magnitude in the same method in Section 4.1 with the correction of IMF from Salpeter IMF to that of what Álvarez-Márquez et al. (2019) use (Chabrier 2003) by dividing stellar mass by 1.74. From the $\beta - M_{UV}$ relation and the estimated stellar mass, L_{UV} is converted into L_{FIR} .

We derive average ρ_{UV} and ρ_{FIR} weighted by the likelihood obtained in the fitting. We employ their minimum and maximum value to estimate the error by varying the parameters of the UVLF/ $\beta - M_{UV}$ relation in the range of their 16th and 84th percentiles, respectively. As a result, we estimate the UV/FIR luminosity density of HSC-SSP protocluster galaxies as $\rho_{UV} = 3.46^{+0.35}_{-0.29} \times 10^{28}$ ($3.53^{+0.17}_{-0.16} \times 10^{28}$) $\text{erg s}^{-1} \text{Hz}^{-1} \text{Mpc}^{-3}$, and $\rho_{FIR} = 1.7^{+0.9}_{-0.9} \times 10^{11}$ ($2.5^{+1.8}_{-1.0} \times 10^{11}$) $L_{\odot} \text{Mpc}^{-3}$ in the case of the Schechter (DPL) function, respectively.

Kubo et al. (2019) conduct stacking analysis of FIR images taken from Planck, AKARI, IRAS, and Herschel at the position of HSC-SSP protoclusters, which is the same sample in this study. Based on their best-fit of the SED model composed of star, dust and AGN flux components, the total FIR luminosity from all galaxies per protocluster is inferred as $L_{FIR} = 1.3^{+1.6}_{-1.0} \times 10^{13} L_{\odot}$. In the case of the SED model without the AGN component, it is estimated as $L_{FIR} = 19.3^{+0.6}_{-4.2} \times 10^{13} L_{\odot}$. As mentioned in Kubo et al. (2019), the best-fit L_{FIR} has degeneracy between two cases, so the uncertainty is quite large. Considering this point and the effective volume of our protoclusters, our estimation of ρ_{FIR} is consistent with these estimations.

For deriving SFRD, We apply the conversion equation from Kennicutt (1998) to ρ_{UV} and ρ_{FIR} , as described below;

$$\text{SFRD} = 1.73 \times 10^{-10} \rho_{FIR} + 1.4 \times 10^{-28} \rho_{UV} \quad (9)$$

As a result, our protocluster galaxies is estimated to have the SFRD corresponding to $\log_{10} \text{SFRD}/(\text{M}_{\odot} \text{yr}^{-1} \text{Mpc}^{-3}) = 1.54^{+0.16}_{-0.20}$ ($1.68^{+0.16}_{-0.17}$) in the case of the Schechter (DPL) function. This value is roughly ~ 2.5 dex higher than that of field galaxies (e.g., $\log_{10} \text{SFRD}/(\text{M}_{\odot} \text{yr}^{-1} \text{Mpc}^{-3}) = -1.00 \pm 0.06$ in Bouwens et al. (2015)), suggesting that our protocluster regions have active star formation.

Previous studies estimate the SFRD of field LBGs by assuming the IRX - β relation of local starburst galaxies in Meurer et al. (1999). For reference, the SFRD of our protocluster members estimated with this IRX- β relation is $\log_{10} \text{SFRD}/(\text{M}_{\odot} \text{yr}^{-1} \text{Mpc}^{-3}) = 1.61^{+0.33}_{-0.45}$ ($1.71^{+0.26}_{-0.31}$) in the case of the Schechter (DPL) function, which is consistent with the original result.

Next, we estimate the fraction of the cosmic SFRD from progenitors of massive halos ($M_{\text{halo}} > 10^{14} M_{\odot}$). We convert the estimated SFRD, which is per unit volume of protocluster, to that per unit of cosmic volume, and divide it by the field SFRD. The field SFRD is taken from [Bouwens et al. \(2015\)](#) ($\log_{10} \text{SFRD}/(M_{\odot} \text{ yr}^{-1} \text{ Mpc}^{-3}) = -1.00 \pm 0.06$). Using other estimates (e.g., [van der Burg et al. 2010](#); [Bouwens et al. 2009](#)) changes the result by only ~ 0.1 dex.

In addition, our protocluster sample is not complete for all progenitors of halos of $M_{\text{halo}} > 10^{14} M_{\odot}$ at $z \sim 0$. Some fraction of dark matter halos with overdensity below 4σ at $z \sim 4$ will also evolve into such halos. We can identify such progenitor halos in the simulation of [Toshikawa et al. \(2018, 2016\)](#). The fraction of halos that can be observed by our protocluster selection with a galaxy overdensity significance greater than 4σ at $z \sim 4$ is about $6.2 \pm 1.0\%$, suggesting that our sample has a very high purity but low completeness. The fraction of halos can be translated to the fraction of member galaxies based on the overdensity distribution of progenitor halos, which is equivalent to $9.67 \pm 0.41\%$. Most of the non-observed member galaxies should be hosted by progenitor halos whose overdensity significance is less than 4σ . With a simple assumption that the UVLF of these galaxies is the same as our PC UVLF, we can derive the intrinsic contribution of progenitor of massive halos to the cosmic SFRD by dividing by this completeness. We mention that the shape of PC UVLF depends on the overdensity, but the main difference of the shape is at $M_{\text{UV}} < -22$, which does not significantly affect the SFRD measurement.

Moreover, 76% of our protocluster sample are expected to evolve into $M_{\text{halo}} > 10^{14} M_{\odot}$ at $z \sim 0$ (T18), so we correct the purity by multiplying this ratio. Finally, we estimate that the $9.4^{+4.7}_{-3.4}\%$ ($13.9^{+6.5}_{-4.9}\%$) of the cosmic SFRD occurs in progenitors of massive halos in the case when we use the best-fit of the Schechter function (the DPL function).

We compare this measurement with the prediction from the SAM in [Chiang et al. \(2017\)](#). They focus on galaxies with $\log(M_*/M_{\odot}) > 8.5$ in progenitors of cluster of $M_{200} > 10^{14} M_{\odot}$ at $z \sim 0$, and estimate that the contribution of protocluster galaxies is about 24 (19)% at $z \sim 4$ when they use [Henriques et al. \(2015\)](#) ([Guo et al. 2013](#)) SAM.

The comparison between the observed and predicted fraction of protocluster galaxies to the cosmic SFRD is shown in Figure 11. Our result is close to the theoretical prediction but slightly smaller. There are two possible explanations. First, we only focus on UV-bright galaxies and miss some other galaxy populations, such as SMGs,

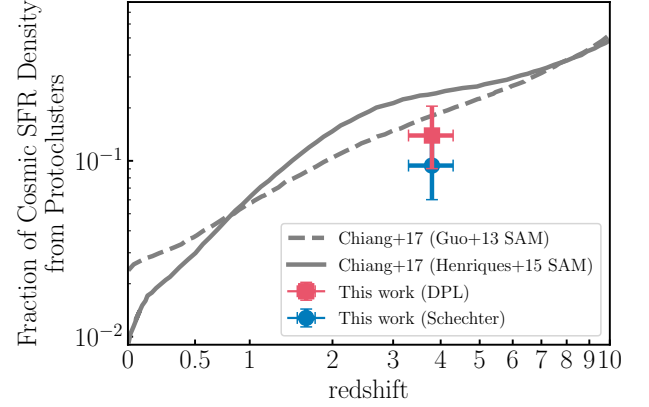


Figure 11. The fraction of the cosmic SFRD in protoclusters. Blue circle and red square represent our estimated value for HSC-SSP protoclusters at $z \sim 4$ assuming that PC UVLF follows Schechter function and DPL function, respectively. Gray solid and dashed lines are its predicted evolution in [Chiang et al. \(2017\)](#) with the use of the semi-analytical model of [Henriques et al. \(2015\)](#) and [Guo et al. \(2013\)](#), respectively.

which are not selected by LBG selection. Though it is not yet clearly understood how much we miss such galaxies by g -dropout selection, [Wang et al. \(2019\)](#) argue that the optically-dark but submillimeter-bright galaxies have a significant contribution to the cosmic SFRD. [Marrone et al. \(2018\)](#) report two SMGs are located in a small separation, implying that they are located in a massive halo. Also, some studies report highly overdense regions of SMGs (e.g., [Miller et al. 2018](#)). Although the FIR luminosity galaxies from [Kubo et al. \(2019\)](#) has a large degeneracy dependent on the SED model they use, the SFRD combined with the UV luminosity density estimated in this work and the stacked FIR luminosity from [Kubo et al. \(2019\)](#) are consistent with the theoretical prediction within the uncertainty. This FIR luminosity, estimated from the stacking, includes the contribution of SMGs, so this does not reject that SMG may be one of the reasons. Second, we may miss some members located on the outskirts of more massive protoclusters. This is because we define protocluster members according to the predicted size of the progenitor of “Fornax-type” clusters, which can be small for progenitors of more massive clusters, like “Coma-like” clusters.

We note that even if we estimate SFRD with the use of the best-fit PC UVLF in the magnitude range of $M_{\text{UV}} < -19$, corresponding to $\log(M_*/M_{\odot}) > 8.5$ according to [Song et al. \(2016\)](#), the result does not change significantly.

5. DISCUSSION

5.1. A Possible Confusion Limit

We have evaluated the sample incompleteness in the same manner as most of the other studies of field LBGs (Section 3.2), and find that it is consistent with previous studies by comparing it with the field UVLF. However, another possible incompleteness could be caused by object confusion in crowded regions, such as in protoclusters. In some overdense regions, some fraction of galaxies will be mixed with nearby objects, which could lower the completeness. Our finding of a flatter UVLF in protoclusters than in the field UVLF could be due to this confusion effect, which might more significantly affect fainter galaxies. The luminosity function shape could change, as seen in this study.

We check this effect by inserting mock galaxies into an overdense region to compare the completeness function in overdense regions with that in the blank field, as estimated in Section 3.2. We summarize the detailed procedure in Appendix D and find that there is no additional incompleteness due to the object confusion in regions with an overdensity significance up to $\sim 8\sigma$.

Though we see a deficit in the faint-end of the PC UVLF compared to the field UVLF, the cause of this will be further investigated in future studies after we construct a protocluster sample in the Deep layer of HSC-SSP, which has deeper image than the Wide layer. However, we now see that the completeness function of g -dropout galaxies estimated in this study is consistent with that of previous studies and that the blending due to focusing on overdense regions like HSC-SSP protoclusters does not lower the completeness. These results imply that the deficit is at least not due to incompleteness.

5.2. Spatial Extension of Protoclusters

We have selected protocluster members from galaxies located within $1.8'$ from each overdensity peak. Since protoclusters with more significant overdensity tend to be more extended, we may miss some protocluster members on the outskirts of protoclusters, and this could lead to the bright-end excess. To examine this possibility, we redefine protocluster members as galaxies which are located within $4.2'$ from the overdensity peak, which corresponds to the size of progenitors of only the most massive halos ($M_{\text{halo}} > 10^{15} M_{\odot}$) like the Coma cluster at $z \sim 4$. We find that the shape of PC UVLF does not change from the case of $1.8'$, suggesting that the trend is not caused by the differences in the typical spatial dimensions of protoclusters of different masses. We also check the case of a smaller protocluster radius ($\sim 1'$) and find that the trend does not change.

5.3. A Possible Excess from the AGN Contribution

Recent studies have argued that the bright-end ($M_{\text{UV}} \leq -23.0$) of the UVLF at $z \sim 4$ is mainly dominated by AGNs (e.g., Adams et al. 2019; Ono et al. 2018). Here, we discuss how well the contribution due to the AGNs can explain the bright-end excess that we found in the PC UVLF for $M_{\text{UV}} \leq -20.8$.

First of all, we compare our PC UVLF to the field quasar UVLF. Akiyama et al. (2018) construct the quasar UVLF at $z \sim 4$. The number density of quasars based on the best-fit DPL function for the magnitude range of $-25.8 < M_{\text{UV}} < -20.8$, which is the range where our PC UVLF has an excess, is about $(0.9 - 10) \times 10^{-7} \text{ Mpc}^{-3} \text{ mag}^{-1}$. This value is $(1 - 240) \times 10^3$ times lower than the excess at the bright-end that we found in the study. In addition, we have found that UV-luminous quasars scarcely exist in the protoclusters at $z \sim 4$ (Uchiyama et al. 2018, in prep.), suggesting that the number density of luminous quasars in protoclusters should not be larger than that in the field.

The difference between PC UVLF and the field UVLF in the magnitude range of $M_{\text{UV}} \leq -20.8$ corresponds to 16 objects per protocluster. The expected total number of members in a protocluster is about 50, indicating that the bright-end excess corresponds to about 32% of the total protocluster members. If we assume that all of the excess at the bright-end is due to the AGN, such a high AGN fraction in protoclusters is inconsistent with previous studies. For example, Toshikawa et al. (2016) make follow-up spectroscopy for protocluster member candidates, and they do not find any AGN in 11 members in a protocluster at $z \sim 3$, suggesting that the AGN fraction is less than 9%. Assuming that the same upper limit for the AGN fraction, the expected number of AGNs in a protocluster is less than five out of 50 members. Other studies show similar AGN fractions for protoclusters from X-ray counterparts. Lehmer et al. (2009) estimate AGN fraction ($9.5_{-6.1}^{+12.7}$ percent) for LBGs in the SSA22 protocluster at $z = 3.09$. Macuga et al. (2019) estimate AGN fraction as $2.0_{-1.3}^{+2.6}$ percent for HAEs in the USS1558-003 protocluster at $z = 2.53$. Krishnan et al. (2017) investigate AGNs in a protocluster called Cl 0218.3-0510 at $z = 1.62$ and estimate that AGN fraction of massive ($\log(M_*/M_{\odot}) > 10$) protocluster galaxies is 17_{-5}^{+6} percent. Though they argue that this value is high compared to that of the blank field at the same redshift, it is not enough to explain the bright-end excess of our PC UVLF. It should be mentioned that the AGN fraction estimated from the X-ray detection can be sensitive to its depth, but these comparison implies that protoclusters at $z \sim 4$ are less likely to host such amount of UV-bright AGNs.

We note that residuals at $M_{UV} < -23.0$ of PC UVLF from the best-fit of the Schechter (DPL) correspond to the 1.5/0.5 objects per protocluster. This seems to be reasonable for the AGN fraction in a protocluster; therefore, a part of the bright-end excess can be contributed by the AGN.

Therefore, we conclude that AGNs are unlikely to explain all of bright-end excess in the PC UVLF. It should be noted that we here discuss the UV-bright AGNs, and we do not include obscured AGNs. As mentioned in Section 4.3, Kubo et al. (2019) stack IR images of various surveys and estimate the total FIR luminosity of the same protocluster sample with this study. Their results imply that HSC-SSP protoclusters can include a population of UV-dim AGNs.

5.4. Galaxy Formation in Overdense Regions

Some studies suggest that the star formation is enhanced in overdense regions at high-redshift compared to in the blank field, as we mentioned in Section 3.4. For example, HAEs in protoclusters at $z \sim 2 - 2.5$ shows an enhancement of high SFR galaxies (Shimakawa et al. 2018; Koyama et al. 2013). In addition, Shi et al. (2019b) report a tentative evidence of higher SFR for Ly α emitting galaxies in protoclusters at $z = 3.13$. On the other hand, local galaxy clusters show the opposite trend. For example, cluster galaxies at $0.18 < z < 0.55$ have SFRs about from $0.00 \pm 0.11 h^{-2} M_{\odot} \text{ yr}^{-1}$ to $0.17 \pm 0.02 h^{-2} M_{\odot} \text{ yr}^{-1}$, which are always lower than those of field galaxies (Balogh et al. 1998). Similarly, the low star formation activity in a cluster is also reported at $z = 1.6$ (Kurk et al. 2009). Combining our results with those from the literature, the enhancement of SFR in overdense environments has already started at $z \sim 4$, and the star formation activity drops at some time between $z \sim 0$ and $z \sim 2$, which is earlier than for field galaxies. This is supported by the fact that massive quiescent galaxies have rapidly emerged in overdense regions in the era from $z \sim 2.5$ to $z \sim 1.5$ (e.g., Wang et al. 2016; Cooke et al. 2015; Newman et al. 2014).

Focusing on the stellar mass, there are several reports that there are more massive galaxies in protoclusters at $z \sim 2 - 3$ (Shimakawa et al. 2018; Koyama et al. 2013; Cooke et al. 2014; Hatch et al. 2011), similar to our results at $z \sim 4$. At lower redshift ($z < 1.5$), the situation is controversial. Many studies report that the shape of the SMFs of star-forming and quiescent galaxies in clusters are similar (e.g., Lin et al. 2017; van der Burg et al. 2013; Calvi et al. 2013), while for those of all cluster galaxies, it is argued that there are significant differences not only in the normalization but also in shape at $z \sim 1$ in van der Burg et al. (2013), at $z \sim 0.5 - 0.7$

in van der Burg et al. (2018) and at $z \sim 0$ in Balogh et al. (2001). In addition, Kovac et al. (2010) report a difference between the SMFs of galaxies in a group environment and those in the blank field. On the other hand, Calvi et al. (2013) suggest that the shape of the SMF is independent of the environment for $z \sim 0$, likewise Nantais et al. (2016) support for $z \sim 1.5$.

It should be noted that some studies report almost no difference from field galaxies in terms of the SFR and stellar mass of protocluster galaxies at $z = 2.9$ (Cucciati et al. 2014), and at $z = 4.57$ (Lemaux et al. 2018). These studies are based on only spectroscopically confirmed members, which are free from contamination, however the sample of members is small (~ 10 objects), which may not reveal the differences that we find on this study based on the statistical sample.

These comparisons suggest that galaxies in overdense regions are more massive and have more active star formation compared to galaxies in the blank field at $z > 1.5$. Whereas at lower redshift, these trends change; galaxies in overdense regions have lower SFR, and the SMF can be identical to that of the field at least when focusing on the same galaxy population. In addition, star-forming galaxies in protoclusters tend to locate at the main sequence at $z \sim 4$ (Long et al. 2020; Shi et al. 2019a), and $z \sim 2 - 2.5$ (Shimakawa et al. 2018; Koyama et al. 2013). This means that the majority of protocluster members are normal galaxies, and the starburst activity is not significant. Therefore, these results may imply the earlier star formation in protoclusters.

This early formation scenario is consistent with theoretical predictions. Chiang et al. (2017) suggest three phases for the evolution of (proto)clusters. Galaxies in protoclusters already begin star formation in an “inside-out” manner from $z \geq 10$ to $z \sim 5$. Then, they continue the star formation from $z \sim 5$ to $z \sim 1.5$. At $z \leq 1.5$, star formation in galaxies is finished, and infalling galaxies into (proto)clusters dominate the main stellar mass growth in protoclusters. Such infalling galaxies are one of the possible reasons that the differences of SMFs of galaxies in local clusters disappear (Vulcani et al. 2013). Steeper SMFs for cluster galaxies at lower- z seen in Section 4.1 can also be explained by this infalling galaxies effect. In addition, they also imply that $\sim 20\%$ of the cosmic SFRD is contributed by protocluster galaxies, which is roughly consistent with our estimation, as discussed in Section 4.3.

The shape difference of the PC UVLF and the PC SMF seen in this study can also be related to frequent mergers or an increase in gas supply towards the center of the connection of several connected filaments in an overdense region, as suggested in Shimakawa et al.

(2018). Indeed, Tomczak et al. (2017) show that “top-heavy” SMFs may originate from the enhancement of mergers in overdense regions. They first construct SMFs for star-forming galaxies and quiescent galaxies at $z \sim 1$ subdivided by their local environment. They find that shapes of SMFs in more overdense regions tend to be more top-heavy. They try to explain this trend by a simple semi-empirical model. This model first generates $\sim 10^6$ galaxies at $z = 5$. For each redshift slice, some fraction of galaxy pairs are selected for the merger, and some fraction of galaxies are selected for quenching. The only free parameter is the merged galaxy fraction. The model shows that the observed SMF in overdense regions can be explained by high-merger rate (80 – 90%). In addition, the increase of gas supply can keep galaxies, which are too massive to be star-forming galaxies in the blank field, to have star-formation. This effect also makes the SMF of protocluster galaxies, which consist only of star-forming ones, to be top-heavy.

We find in Section 4.2 that all protoclusters follow the same trend that galaxies in more massive overdense regions tend to have a flatter UVLF, though the diversity exists even if we focus on protoclusters with the same overdensity. The trend implies that more massive regions have generally experienced the earlier structure formation, but their evolutionary stage has a significant variation even at the same epoch. This indicates that a large sample at each redshift is critically essential for tracing the general evolutionary sequence of protoclusters within this diversity.

6. CONCLUSION

In this paper, we report the rest-UV luminosity function of g -dropout galaxies in 177 protocluster candidates (PC UVLF) at $z \sim 4$ detected in the HSC-SSP data. The PC UVLF is estimated in the magnitude range of $-25.8 \leq M_{UV} \leq -20.3$ after subtracting for the contamination from field galaxies.

1. Compared to the UVLF of galaxies in the blank field, the PC UVLF has a significant excess towards the bright-end in addition to a higher normalization. The best-fit parameters of both the Schechter functions and DPL functions for the PC UVLF also reveal the shape differences from that of the field. The excess towards the bright-end implies that the SFR of galaxies in overdense regions must have accelerated at $z \geq 4$.
2. Assuming that all protocluster galaxies follow the “main sequence” of star-forming galaxies, we convert the PC UVLF to the SMF. Protocluster galaxies are inferred to have 2.8 times more massive characteristic stellar mass than their field

counterparts at the same epoch. We show that protocluster galaxies have to continue their stellar mass growth to match SMFs of (proto)cluster galaxies at lower redshift.

3. More massive protoclusters tend to have a higher bright-end amplitude in the UVLF, although the variation is seen even if we only focus on protoclusters with the same overdensity. The bright-end excess is ubiquitously seen in most of protoclusters at $z \sim 4$.
4. Protoclusters have the enhanced SFRD as $\log_{10} \text{SFRD}/(\text{M}_{\odot} \text{ yr}^{-1} \text{ Mpc}^{-3}) = 1.54^{+0.16}_{-0.20} (1.68^{+0.16}_{-0.17})$ using the best-fit of Schechter (DPL) function. This corresponds to the 6 – 20% of the cosmic SFRD, being close to the theoretical prediction of Chiang et al. (2017), but somewhat smaller. This difference from the prediction might be due to the ignorance of SMG in this study and the missed protocluster members located at the edges of protoclusters.

Highly star forming and more massive galaxies in protoclusters are reported in protoclusters at lower redshift. We interpret this trend as a signature of the fact that protoclusters are regions in the cosmic web where galaxies and structures form earlier.

In this paper, we only focus on protoclusters at $z \sim 4$. Currently, we are in the process of selecting protocluster candidates at $z \sim 2 - 6$ from HSC-SSP data in the systematic way same as in T18. This will enable us to determine the UVLF and SFRD of protocluster galaxies at different redshifts and hence trace their redshift evolution.

We acknowledge Dr. Masao Hayashi for providing the instruction for the detection of mock galaxies by using `hscpipe`. Also, we appreciate the anonymous referee for helpful comments and suggestions that improved the manuscript.

This work was partially supported by Overseas Travel Fund for Students (2019) of the Department of Astronomical Science, the Graduate University for Advanced Studies (SOKENDAI).

The Hyper Suprime-Cam (HSC) collaboration includes the astronomical communities of Japan and Taiwan, and Princeton University. The HSC instrumentation and software were developed by the National Astronomical Observatory of Japan (NAOJ), the Kavli Institute for the Physics and Mathematics of the Universe (Kavli IPMU), the University of Tokyo, the High Energy Accelerator Research Organization (KEK), the

Academia Sinica Institute for Astronomy and Astrophysics in Taiwan (ASIAA), and Princeton University. Funding was contributed by the FIRST program from the Japanese Cabinet Office, the Ministry of Education, Culture, Sports, Science and Technology (MEXT), the Japan Society for the Promotion of Science (JSPS), Japan Science and Technology Agency (JST), the Toray Science Foundation, NAOJ, Kavli IPMU, KEK, ASIAA, and Princeton University.

This paper makes use of software developed for the Large Synoptic Survey Telescope. We thank the LSST Project for making their code available as free software at <http://dm.lsst.org>.

This paper is based on data collected at the Subaru Telescope and retrieved from the HSC data archive system, which is operated by Subaru Telescope and Astronomy Data Center (ADC) at NAOJ. Data analysis was in part carried out with the cooperation of Center for Computational Astrophysics (CfCA), NAOJ.

The Pan-STARRS1 Surveys (PS1) and the PS1 public science archive have been made possible through contributions by the Institute for Astronomy, the University of Hawaii, the Pan-STARRS Project Office, the Max Planck Society and its participating institutes, the Max Planck Institute for Astronomy, Heidelberg, and the Max Planck Institute for Extraterrestrial Physics, Garching, The Johns Hopkins University, Durham University, the University of Edinburgh, the Queen's University Belfast, the Harvard-Smithsonian Center for Astrophysics, the Las Cumbres Observatory Global Telescope Network Incorporated, the National Central University of Taiwan, the Space Telescope Science Institute, the National Aeronautics and Space Administration under grant No. NNX08AR22G issued through the Planetary Science Division of the NASA Science Mission Directorate, the National Science Foundation grant No. AST-1238877, the University of Maryland, Eotvos Lorand University (ELTE), the Los Alamos National Laboratory, and the Gordon and Betty Moore Foundation.

Facilities: Subaru (HSC)

APPENDIX

A. THE IMPACT OF THE PHOTOMETRIC UNCERTAINTY ON THE SHAPE OF THE PC UVLF

Here, we examine the effect of the photometric uncertainty on the shape of the UVLF.

We first check the uncertainty of the PC UVLF due to the photometric uncertainty. For each galaxy, we generate mock M_{UV} by adding Gaussian noise whose 1σ corresponds to the observed photometric error to the observed magnitude. The PC UVLF is recalculated from this M_{UV} distribution with the 1000 times iteration. The right panel of Figure 12 shows the recalculated PC UVLF (called pseudo PC UVLF) compared with the original PC UVLF. These two UVLFs are consistent, so this implies that the uncertainty of the PC UVLF due to the photometric uncertainty is negligible.

We then assess the Eddington Bias. We first derive the difference between the original magnitude and that with artificially noise, estimated in the previous paragraph. Followed by the method in the previous works (e.g., Ilbert et al. 2013) which estimate the effect of the Eddington Bias to the stellar mass function, the product of the Gaussian distribution $G(x) = \frac{1}{\sigma\sqrt{2\pi}} \exp(-\frac{1}{2}\frac{x^2}{\sigma^2})$ and the Lorentzian distribution $L(x) = \frac{\tau}{2\pi} \frac{1}{(\frac{\tau}{2})^2 + x^2}$ is fitted to the magnitude difference distribution, which is shown in the left panel of Figure 12, and we obtain the best-fit parameters (σ and τ). Convolution of the observed field UVLF with the best-fit functions provides us how significant the Eddington bias is in our photometry quality. Here, we employ the best-fit Schechter function of the field UVLF obtained in Ono et al. (2018).

The right panel of Figure 12 shows the convolved field UVLF. Compared with the original field UVLF, it has indeed slightly higher amplitude than the original one, but it has still steep shape than our estimated PC UVLF. This implies that the our photometric quality does not make the bright-end excess seen in the PC UVLF from the field UVLF.

B. THE PC UVLF IN THE CASE OF $F(M_{UV}) = 1$

We compare the PC UVLF when we set the volume ratio factor $F(M_{UV}) = 1$ in Equation 4 with the PC UVLF and the field UVLF (Ono et al. 2018). This PC UVLF still has the bright-end excess compared to the field UVLF, as seen in Figure 13.

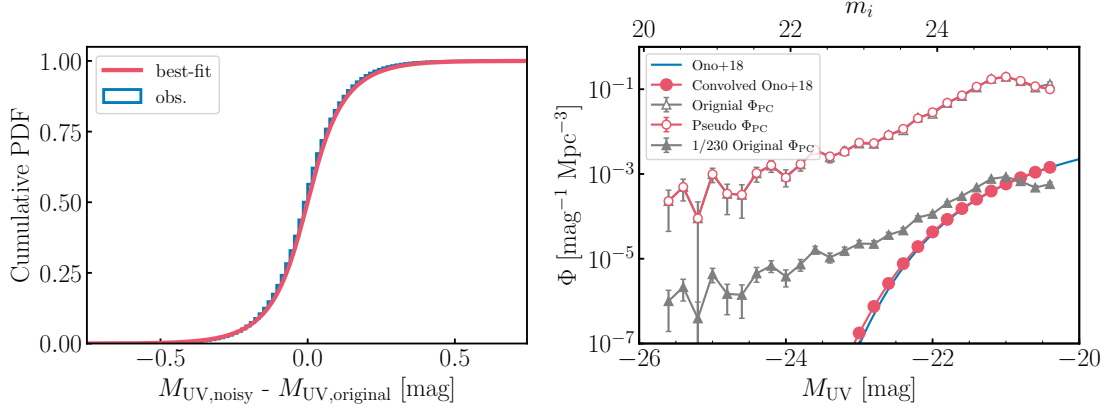


Figure 12. Left panel: The distribution of the difference between the original magnitude and the noise added one, which is shown as blue histogram. The best-fit of the product of the Gaussian distribution and the Lorentzian distribution is shown in the red line. Right panel: The convolved (red filled circles) and original (blue line) field UVLF (Ono et al. 2018) and the shifted (gray triangles), pseudo (red open circles), and original (gray open triangles) PC UVLF in this work.

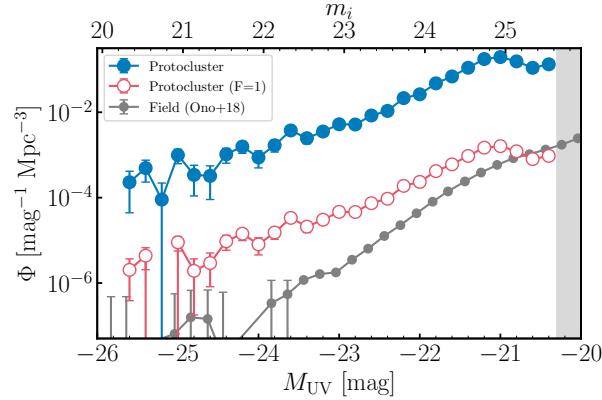


Figure 13. The PC UVLF in the case of $F(M_{UV}) = 1$ (open red circles) and the original PC UVLF (filled blue circles). For comparison, the field UVLF (Ono et al. 2018) is plotted in a gray line.

C. THE ROBUSTNESS OF UV SLOPE-MAGNITUDE RELATION

To assess the robustness of our measurement of UV-slope β and the sample selection, we measure the β of field galaxies in the same manner as described in Section 4.2 to compare it with the relation in the literature. The $\beta - M_{UV}$ relation for our field galaxies as well as in the literature (Bouwens et al. 2014, 2009) are shown in Figure 14. Our $\beta - M_{UV}$ relation for field galaxies is consistent with the literature at $-22.3 < M_{UV} < -20.3$, suggesting that our measurement and the sample selection is robust.

D. COMPLETENESS AFFECTED BY A POSSIBLE CONFUSION LIMIT AT OVERDENSE REGIONS

In this paper, we focus on overdense regions of galaxies. In such regions, the image blending of galaxies might frequently occur due to the high local number density and this could lead to an inaccurate photometry of galaxies. The blending also could decrease the sample completeness. This effect is closely related to the number density of galaxies that we focus on. Here, we examine how significantly the blending effect affects the photometry and the completeness by inserting mock galaxies on the image to make artificial overdense regions.

Firstly, we make a cut out image with $4' \times 4'$ of an overdense region whose overdensity peak is about 3σ . In Toshikawa et al. (2018), the average and the standard deviation of the number of bright ($m_i < 25$ mag) galaxies within $1''.8$ are 6.4 and 3.2, respectively. According to the field luminosity function of g -dropout galaxies (e.g., Ono et al. 2018), this implies that 1σ of the number density of galaxies with $25 < m_i < 26$ is about $1.8 \text{ mag}^{-1} \text{ arcmin}^{-2}$. We make five artificial

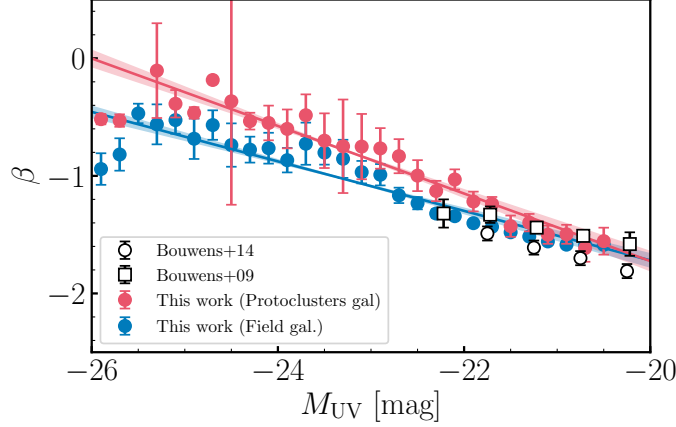


Figure 14. The $\beta - M_{UV}$ relations estimated in this study. The red circles represent the median value of UV slope of protocluster galaxies and the red line represents its best-fit. The blue circles and the blue line represent those of field galaxies. The shaded regions of each best-fit lines represent their 1σ uncertainty. Relations from the literature (Bouwens et al. 2014, 2009) is also shown, our estimation for field galaxies is consistent with it, suggesting the robustness of our UV slope estimation.

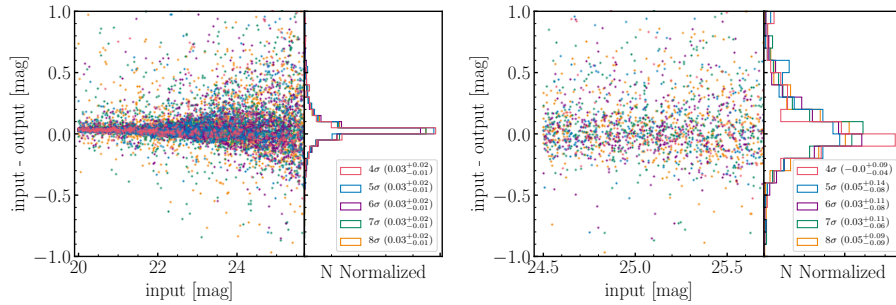


Figure 15. The comparison of the input magnitude and the output magnitude of mock galaxies. Red, blue, purple, green, and yellow markers show cases in 4σ , 5σ , 6σ , 7σ , 8σ regions. The left panel plots all detected mock galaxies, and the right panel plots only faint galaxies with $m_i > 24.5$. In each panel, the median value and 16/84th percentile uncertainty is shown, and all of them is consistent, suggesting that the blending due to the overdensity does not affect the photometry.

overdense region image by inserting mock galaxies to the cutout image so that their number densities are equivalent to 1.8, 3.6, 5.4, 7.2, and 9.0 $\text{arcmin}^{-2}\text{mag}^{-1}$, corresponding to the overdensity significance of 4σ , 5σ , 6σ , 7σ , and 8σ , respectively, which is the same overdensity range of our protocluster sample. The morphological and physical properties of mock galaxies are the same as that we did in estimating the completeness in Section 3.2. We fix the redshift as $z = 3.8$ since we only aim to see the difference induced by the number density of galaxies in the field. The detection and the measurement process are also the same as that described in Section 3.2.

We compare the output magnitude of the detected objects from `hscpipe` to the input magnitude of mock galaxies in Figure 15. The magnitude difference between the input and output magnitude are consistent at any overdensities. The peak difference between the input and the output magnitude is lower than the photometric error, suggesting that the magnitudes are accurately recovered. This result implies that the photometry is not affected by the blending due to the overdensity. Even we only focus on faint ($m_i > 24.5$) objects, which can be more blended by other bright objects, they also follow the same trend (the right panel of Figure 15).

As same in Section 3.2, we construct a completeness function as a function of magnitude. Figure 16 shows the ratio between these completeness function and that at $z = 3.8$ estimated in Section 3.2. The ratio do not change around one up to 8σ . This suggests that the overdensity in the range of that of our protoclusters does not affect the completeness function.

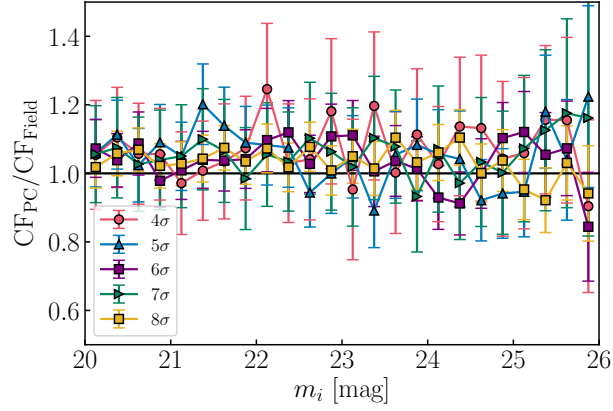


Figure 16. The ratio of the completeness function in overdense regions to that in the blank field. Red, blue, purple, green, and yellow lines correspond to cases in 4σ , 5σ , 6σ , 7σ , 8σ regions, respectively. Error bars represent the Poisson error of the number of detected mock galaxies for each bins.

REFERENCES

- Adams, N. J., Bowler, R. A. A., Jarvis, M. J., et al. 2019, arXiv.org, arXiv:1912.01626
- Aihara, H., Arimoto, N., Armstrong, R., et al. 2018a, PASJ, 70, S4
- Aihara, H., Armstrong, R., Bickerton, S., et al. 2018b, PASJ, 70, S8
- Akiyama, M., He, W., Ikeda, H., et al. 2018, PASJ, 70, S34
- Alam, S., Albareti, F. D., Allende Prieto, C., et al. 2015, ApJS, 219, 12
- Álvarez-Márquez, J., Burgarella, D., Buat, V., Ilbert, O., & Pérez-González, P. G. 2019, A&A, 630, A153
- Axelrod, T., Kantor, J., Lupton, R. H., & Pierfederici, F. 2010, in Proceedings of the SPIE, ed. N. M. Radziwill & A. Bridger, Steward Observatory, United States (SPIE), 774015
- Balogh, M. L., Christlein, D., Zabludoff, A. I., & Zaritsky, D. 2001, ApJ, 557, 117
- Balogh, M. L., Schade, D., Morris, S. L., et al. 1998, ApJ, 504, L75
- Bamford, S. P., Nichol, R. C., Baldry, I. K., et al. 2008, arXiv.org, 1324
- Bertin, E. 2011, in Astronomical Data Analysis Software and Systems XX. ASP Conference Proceedings, 435–
- Biviano, A., Moretti, A., Paccagnella, A., et al. 2017, A&A, 607, A81
- Boquien, M., Burgarella, D., Roehlly, Y., et al. 2019, A&A, 622, A103
- Bosch, J., Armstrong, R., Bickerton, S., et al. 2018, PASJ, 70, S5
- Bouwens, R. J., Illingworth, G. D., Franx, M., et al. 2009, ApJ, 705, 936
- Bouwens, R. J., Illingworth, G. D., Oesch, P. A., et al. 2012, ApJ, 754, 83
- . 2014, ApJ, 793, 115
- . 2015, ApJ, 803, 34
- Bowler, R. A. A., Jarvis, M. J., Dunlop, J. S., et al. 2019, arXiv.org
- Bowler, R. A. A., Dunlop, J. S., McLure, R. J., et al. 2015, MNRAS, 452, 1817
- Bruzual, G., & Charlot, S. 2003, MNRAS, 344, 1000
- Cai, Z., Fan, X., Peirani, S., et al. 2016, ApJ, 833, 135
- Calvi, R., Poggianti, B. M., Vulcani, B., & Fasano, G. 2013, MNRAS, 432, 3141
- Calzetti, D., Armus, L., Bohlin, R. C., et al. 2000, ApJ, 533, 682
- Chabrier, G. 2003, ApJ, 586, L133
- Chiang, Y.-K., Overzier, R. A., & Gebhardt, K. 2013, ApJ, 779, 127
- . 2014, ApJL, 782, L3
- Chiang, Y.-K., Overzier, R. A., Gebhardt, K., & Henriques, B. 2017, ApJL, 844, L23
- Cooke, E. A., Hatch, N. A., Muldrew, S. I., Rigby, E. E., & Kurk, J. D. 2014, MNRAS, 440, 3262
- Cooke, E. A., Hatch, N. A., Rettura, A., et al. 2015, MNRAS, 452, 2318
- Cucciati, O., Tresse, L., Ilbert, O., et al. 2012, A&A, 539, A31
- Cucciati, O., Zamorani, G., Lemaux, B. C., et al. 2014, A&A, 570, A16
- Davidzon, I., Ilbert, O., Laigle, C., et al. 2017, A&A, 605, A70
- Demarco, R., Wilson, G., Muzzin, A., et al. 2010, ApJ, 711, 1185

- Dressler, A. 1980, *ApJ*, 236, 351
- Eddington, A. S. 1913, *MNRAS*, 73, 359
- Fasano, G., Marmo, C., Varela, J., et al. 2006, *A&A*, 445, 805
- Finkelstein, S. L., Ryan, R. E. J., Papovich, C., et al. 2015, *ApJ*, 810, 71
- Garilli, B., Guzzo, L., Scodeggio, M., et al. 2014, *Astronomy & Astrophysics*, 562, A23
- Guo, Q., White, S., Angulo, R. E., et al. 2013, *MNRAS*, 428, 1351
- Hatch, N. A., Kurk, J. D., Pentericci, L., et al. 2011, *MNRAS*, 415, 2993
- Hayashi, M., Kodama, T., Tadaki, K.-i., Koyama, Y., & Tanaka, I. 2012, *ApJ*, 757, 15
- Henriques, B. M. B., White, S. D. M., Thomas, P. A., et al. 2015, *MNRAS*, 451, 2663
- Higuchi, R., Ouchi, M., Ono, Y., et al. 2019, *ApJ*, 879, 28
- Hogg, D. W. 1999, *arXiv.org*, *arXiv:astro*
- Ilbert, O., McCracken, H. J., Le Fevre, O., et al. 2013, *A&A*, 556, A55
- Ito, K., Kashikawa, N., Toshikawa, J., et al. 2019, *ApJ*, 878, 68
- Ivezić, Ž., Kahn, S. M., Tyson, J. A., et al. 2008, *arXiv.org*, *arXiv:0805.2366*
- Jiang, L., Wu, J., Bian, F., et al. 2018, *Nature Astronomy*, 2, 962
- Jurić, M., Kantor, J., Lim, K. T., et al. 2015, *arXiv.org*
- Kawanomoto, S., Uruguchi, F., Komiyama, Y., et al. 2018, *PASJ*, 70, 66
- Kennicutt, R. C. J. 1998, *ARA&A*, 36, 189
- Komiyama, Y., Obuchi, Y., Nakaya, H., et al. 2018, *PASJ*, 70, S2
- Konno, A., Ouchi, M., Nakajima, K., et al. 2016, *ApJ*, 823, 20
- Kovac, K., Lilly, S. J., Knobel, C., et al. 2010, *ApJ*, 718, 86
- Koyama, Y., Kodama, T., Tadaki, K.-i., et al. 2013, *MNRAS*, 428, 1551
- Krishnan, C., Hatch, N. A., Almaini, O., et al. 2017, *MNRAS*, 470, 2170
- Kubo, M., Toshikawa, J., Kashikawa, N., et al. 2019, *ApJ*, 887, 214
- Kurk, J., Cimatti, A., Zamorani, G., et al. 2009, *A&A*, 504, 331
- Lee, K.-G., Hennawi, J. F., White, M., Croft, R. A. C., & Ozbek, M. 2014, *ApJ*, 788, 49
- Lee, K.-G., Hennawi, J. F., White, M., et al. 2016, *ApJ*, 817, 160
- Lehmer, B. D., Alexander, D. M., Geach, J. E., et al. 2009, *ApJ*, 691, 687
- Lemaux, B. C., Le Fevre, O., Cucciati, O., et al. 2018, *A&A*, 615, A77
- Lidman, C., Suherli, J., Muzzin, A., et al. 2012, *MNRAS*, 427, 550
- Lin, Y.-T., Hsieh, B.-C., Lin, S.-C., et al. 2017, *ApJ*, 851, 139
- Long, A. S., Cooray, A., Ma, J., et al. 2020, *arXiv.org*
- Lovell, C. C., Thomas, P. A., & Wilkins, S. M. 2018, *MNRAS*, 474, 4612
- Lovell, C. C., Vijayan, A. P., Thomas, P. A., et al. 2020, *arXiv.org*
- Macuga, M., Martini, P., Miller, E. D., et al. 2019, *ApJ*, 874, 54
- Madau, P., & Dickinson, M. 2014, *ARA&A*, 52, 415
- Marrone, D. P., Spilker, J. S., Hayward, C. C., et al. 2018, *Nature*, 553, 51
- Meiksin, A. 2006, *MNRAS*, 365, 807
- Meurer, G. R., Heckman, T. M., & Calzetti, D. 1999, *ApJ*, 521, 64
- Miller, T. B., Chapman, S. C., Aravena, M., et al. 2018, *Nature*, 556, 469
- Miyazaki, S., Komiyama, Y., Kawanomoto, S., et al. 2018, *PASJ*, 70, S1
- Muldrew, S. I., Hatch, N. A., & Cooke, E. A. 2015, *MNRAS*, 452, 2528
- Muzzin, A., Wilson, G., Yee, H. K. C., et al. 2009, *ApJ*, 698, 1934
- Nantais, J. B., van der Burg, R. F. J., Lidman, C., et al. 2016, *A&A*, 592, A161
- Newman, A. B., Ellis, R. S., Andreon, S., et al. 2014, *ApJ*, 788, 51
- Oguri, M., Lin, Y.-T., Lin, S.-C., et al. 2018, *PASJ*, 70, S20
- Ono, Y., Ouchi, M., Harikane, Y., et al. 2018, *PASJ*, 70, S10
- Onoue, M., Kashikawa, N., Uchiyama, H., et al. 2018, *PASJ*, 70, S31
- Ouchi, M., Shimasaku, K., Akiyama, M., et al. 2005, *ApJ*, 620, L1
- Overzier, R. A. 2016, *A&A Rv*, 24, 14
- Overzier, R. A., Bouwens, R. J., Cross, N. J. G., et al. 2008, *ApJ*, 673, 143
- Rowe, B. T. P., Jarvis, M., Mandelbaum, R., et al. 2015, *Astronomy and Computing*, 10, 121
- Salpeter, E. E. 1955, *ApJ*, 121, 161
- Schechter, P., & Press, W. H. 1976, *ApJ*, 203, 557
- Schlegel, D. J., Finkbeiner, D. P., & Davis, M. 1998, *ApJ*, 500, 525
- Sérsic, J. L. 1963, *Boletin de la Asociacion Argentina de Astronomia*, 6, 41
- Shi, K., Lee, K.-S., Dey, A., et al. 2019a, *ApJ*, 871, 83
- Shi, K., Huang, Y., Lee, K.-S., et al. 2019b, *ApJ*, 879, 9

- Shibuya, T., Ouchi, M., & Harikane, Y. 2015, *ApJS*, 219, 15
- Shimakawa, R., Kodama, T., Hayashi, M., et al. 2018, *MNRAS*, 473, 1977
- Sohn, J., Geller, M. J., Rines, K. J., et al. 2018, *ApJ*, 856, 172
- Song, M., Finkelstein, S. L., Ashby, M. L. N., et al. 2016, *ApJ*, 825, 5
- Speagle, J. S., Steinhardt, C. L., Capak, P. L., & Silverman, J. D. 2014, *ApJS*, 214, 15
- Stark, C. W., Font-Ribera, A., White, M., & Lee, K.-G. 2015, *MNRAS*, 453, 4311
- Steidel, C. C., Adelberger, K. L., Dickinson, M., et al. 1998, *ApJ*, 492, 428
- Steidel, C. C., Adelberger, K. L., Shapley, A. E., et al. 2005, *ApJ*, 626, 44
- Suchyta, E., Huff, E. M., Aleksić, J., et al. 2016, *MNRAS*, 457, 786
- Tanaka, M., Valentino, F., Toft, S., et al. 2019, *ApJL*, 885, L34
- Thomas, D., Maraston, C., Bender, R., & Mendes de Oliveira, C. 2005, *ApJ*, 621, 673
- Tomczak, A. R., Quadri, R. F., Tran, K.-V. H., et al. 2016, *ApJ*, 817, 118
- Tomczak, A. R., Lemaux, B. C., Lubin, L. M., et al. 2017, *MNRAS*, 472, 3512
- Toshikawa, J., Malkan, M. A., Kashikawa, N., et al. 2020, *The Astrophysical Journal*, 888, 89
- Toshikawa, J., Kashikawa, N., Ota, K., et al. 2012, *ApJ*, 750, 137
- Toshikawa, J., Kashikawa, N., Overzier, R. A., et al. 2016, *ApJ*, 826, 114
- Toshikawa, J., Uchiyama, H., Kashikawa, N., et al. 2018, *PASJ*, 70, S12
- Uchiyama, H., Toshikawa, J., Kashikawa, N., et al. 2018, *PASJ*, 70, S32
- Valentino, F., Tanaka, M., Davidzon, I., et al. 2020, *ApJ*, 889, 93
- van der Burg, R. F. J., Hildebrandt, H., & Erben, T. 2010, *A&A*, 523, A74
- van der Burg, R. F. J., McGee, S., Aussel, H., et al. 2018, *A&A*, 618, A140
- van der Burg, R. F. J., Muzzin, A., Hoekstra, H., et al. 2013, *A&A*, 557, A15
- Venemans, B. P., Kurk, J. D., Miley, G. K., et al. 2002, *ApJ*, 569, L11
- Venemans, B. P., Röttgering, H. J. A., Miley, G. K., et al. 2007, *A&A*, 461, 823
- Vulcani, B., Poggianti, B. M., Oemler, A., et al. 2013, *A&A*, 550, A58
- Wang, T., Elbaz, D., Daddi, E., et al. 2016, *ApJ*, 828, 56
- Wang, T., Schreiber, C., Elbaz, D., et al. 2019, *Nature*, 572, 211
- Wilson, G., Muzzin, A., Yee, H. K. C., et al. 2009, *ApJ*, 698, 1943
- Yoshida, M., Shimasaku, K., Kashikawa, N., et al. 2006, *ApJ*, 653, 988